CrossMark

J. Fluid Mech. (2016), *vol.* 802, *pp.* 108–146. © Cambridge University Press 2016
doi:10.1017/jfm.2016.313

Rapid distortion theory analysis on the interaction between homogeneous turbulence and a planar shock wave

T. Kitamura[1,†], K. Nagata[2], Y. Sakai[1], A. Sasoh[2] and Y. Ito[1]

[1]Department of Mechanical Science and Engineering, Nagoya University, Nagoya, Aichi 464-8603, Japan

[2]Department of Aerospace Engineering, Nagoya University, Nagoya, Aichi 464-8603, Japan

(Received 2 August 2015; revised 18 April 2016; accepted 2 May 2016;
first published online 1 August 2016)

The interactions between homogeneous turbulence and a planar shock wave are analytically investigated using rapid distortion theory (RDT). Analytical solutions in the solenoidal modes are obtained. Qualitative answers to unsolved questions in a report by Andreopoulos *et al.* (*Annu. Rev. Fluid Mech.*, vol. 524, 2000, pp. 309–345) are provided within the linear theoretical framework. The results show that the turbulence kinetic energy (TKE) is increased after interaction with a shock wave and that the contributions to the amplification can be interpreted primarily as the combined effect of shock-induced compression, which is a direct consequence of the Rankine–Hugoniot relation, and the nonlinear effect, which is an indirect consequence of the Rankine–Hugoniot relation via the perturbation manner. For initial homogeneous axisymmetric turbulence, the amplification of the TKE depends on the initial degree of anisotropy. Furthermore, the increase in energy at high wavenumbers is confirmed by the one-dimensional spectra. The enstrophy is also increased; its increase is more significant than that of the TKE because of the significant increase in enstrophy at high wavenumbers. The vorticity components perpendicular to the shock-induced compressed direction are amplified more than the parallel vorticity component. These results strongly suggest that a high resolution is needed to obtain accurate results for the turbulence–shock-wave interaction. The integral length scales (L) and the Taylor microscales (λ) are decreased for most cases after the interaction. However, $L_{22,3}(=L_{33,2})$ and $\lambda_{22,3}(=\lambda_{33,2})$ are amplified. Here, the subscripts 2 and 3 indicate the perpendicular components relative to the shock-induced compressed direction. The dissipation length and TKE dissipation rate are amplified.

Key words: homogeneous turbulence, shock waves

1. Introduction

The interaction between turbulence and a shock wave is very important in engineering and space physics. This interaction is observed in supersonic transport (SST) in the generation of sonic booms and in the flow of a combustor in engineering.

† Email address for correspondence: turbulence.t.k.0426@gmail.com

https://doi.org/10.1017/jfm.2016.313 Published online by Cambridge University Press

Turbulence–shock interactions are observed in space physics, such as in star formation, with supernovas, and in the interaction between solar wind and bow shock around the Earth.

With fluids in space, the characteristics of Burgulence, in which the velocity spectrum exhibits $E(k) \sim k^{-2}$, have been observed in the Ursa Major interstellar cloud (Miville-Deschenes *et al.* 2003), where k is the wavenumber. On the other hand, the characteristic of Kolmogorov turbulence, the spectrum of electron density fluctuations $k^2 N_k^{(e)}(k) \sim k^{-5/3}$, has been observed in the local interstellar medium (Armstrong, Rickett & Spranger 1995). Here, $N_k^{(e)}(k)$ is an electron density power spectrum. The former is considered to be a characteristic in which the dilatational mode dominates the velocity field, whereas the latter corresponds to the case in which the solenoidal mode dominates the velocity field. The change in turbulence interacted with a shock wave is assumed to depend on which mode dominated before the interaction.

A fundamental understanding of such physics is necessary for the development of next generation SSTs, improvement of combustion processes and high-speed rotor flows, and for an understanding of space physics. However, it is difficult to comprehend the relationships between turbulence and a shock wave. In fact, complex linear and nonlinear mechanisms are involved, which can cause considerable changes in the structure of turbulence and its statistical properties, and alter the dynamics of the shock wave motion (Andreopoulos, Agui & Briassulis 2000). Amplification of velocity fluctuations and substantial changes in turbulence characteristic length scales are the most important outcomes of the interaction of turbulence with a shock wave. However, there have been qualitative and quantitative disagreements between experimental results and direct numerical simulation (DNS) results in previous studies, and the lack of a theory on the interaction between turbulence and shock waves has been identified.

Andreopoulos *et al.* (2000) documented the following unanswered questions regarding the interaction between turbulence and shock waves from the perspective of turbulence research.

(i) How much of the amplification of turbulence interacted with a shock wave is caused entirely by the Rankine–Hugoniot conditions?
(ii) Why are vorticity fluctuations amplified more than velocity fluctuations?
(iii) Why is the energy of small eddies amplified more than that of large eddies?
(iv) Are the length scales of the incoming turbulence reduced or amplified through these interactions?
(v) Is the turbulence kinetic energy (TKE) dissipation rate reduced?

This paper attempts to provide analytical answers to the above five questions using rapid distortion theory (RDT) analysis.

Direct numerical simulations on the interaction between homogeneous isotropic turbulence (HIT) and a standing shock wave, and experiments on the interaction between grid turbulence and a moving shock wave have been conducted to deepen the fundamental understanding of these phenomena. Using DNS, Lee, Lele & Moin (1993) and Hannappel & Friedrich (1995) showed that all turbulence characteristic lengths (i.e. longitudinal and lateral velocity integral length scale, longitudinal and lateral velocity Taylor microscale, dissipation length scale, and the integral length scales and Taylor microscales of density fluctuations) are decreased after the interaction. Lee, Lele & Moin (1997) showed that the turbulence dissipation scale is increased after interaction with a strong shock wave. Mahesh, Lele & Moin (1997) showed that upstream entropy fluctuations and the velocity–temperature correlation have a strong influence on the turbulence evolution across a shock wave. They also found

https://doi.org/10.1017/jfm.2016.313 Published online by Cambridge University Press

higher amplifications of the TKE and enstrophy when the upstream turbulence has a negative velocity–temperature correlation, whereas the amplifications are lower when the upstream turbulence has a positive velocity–temperature correlation. Larsson & Lele (2009) and Larsson, Bermejo-Moreno & Lele (2013) showed that the criterion for the 'wrinkled' and 'broken' shock regimes is characterized by $M_t/(M_s-1)$, where M_t and M_s are the turbulent Mach number and the shock Mach number respectively. One important consequence of the effect of M_t is that a shock wave tends to be broken with an increase of $M_t/(M_s-1)$ (Larsson & Lele 2009; Larsson *et al.* 2013). Larsson & Lele (2009) showed that the amplification of vorticity fluctuations strongly depends on the grid resolution. Larsson *et al.* (2013) also showed that the evolution of the TKE is damped and that the TKE evolves to have a peak located at $0.8L_\epsilon$ behind a shock wave, where L_ϵ is the dissipation length scale. Grube, Taylor & Martin (2011) showed that the evolution of the TKE is approximately monotonic without the damping and that the compressible contribution is much larger than other contributions for the transverse vorticity variance budget.

Keller & Merzkirch (1990) conducted experiments on the interaction between compressible grid turbulence and a reflected shock wave, and measured density fluctuations using the speckle method. Then, they showed that the longitudinal integral length scale and Taylor microscale of density fluctuations were amplified after the interaction. Honkan & Andreopoulos (1992) conducted shock-tube experiments and showed that the streamwise root mean square (r.m.s.) velocity was amplified and that the energy at large scales (rather than that at small scales) was amplified; the turbulence dissipation scale was also increased. On the other hand, Briassulis *et al.* (1996) showed that the eddies are significantly compressed in the longitudinal direction, whereas their extent in the normal direction remains similar for weak interactions; the eddies are compressed in both directions for strong interactions. Agui, Briassulis & Andreopoulos (2005) conducted experiments on grid turbulence and a moving shock wave in a large shock-tube facility. They investigated the statistical quantities related to vorticity using a vorticity probe and showed that the vorticity components perpendicular to the shock wavefront increase and that the streamwise integral length scale decreases after the interaction. Regarding the TKE dissipation rate, they found that the solenoidal dissipation occupies more than the dilatational dissipation throughout the interaction, and that the TKE dissipation rate is amplified after the interaction. Barre, Alem & Bonnet (1996) conducted experiments on the interaction between Mach 3 quasi-isotropic turbulence and a standing shock wave, and showed that the amplification of the variance of the streamwise velocity fluctuation, the strong anisotropy behind a shock wave, and the decrease in the streamwise integral length scales by up to $1/7$ after the interaction.

Thus, although all previous studies have shown amplification of the TKE based on interactions with a shock wave, the question as to whether the turbulence characteristic scale increases or decreases remains unsolved because there has been little agreement in previous studies.

In theoretical studies of the amplification of velocity fluctuations when interacting with a shock wave, there are two main methods: the linear interaction approximation (LIA) and RDT. Lee *et al.* (1993) showed that the Taylor microscale is decreased after interaction with a shock wave using the LIA. On the other hand, RDT is a valid method in the case of rapid distortion of turbulent structures such as interaction with a shock wave. In RDT, either Cartesian coordinates or Craya–Herring coordinates are used. The former are able to compare the results directly with experiments and DNS. The latter are convenient for interpretation and are easy to calculate. Jacquin, Cambon & Blin (1993) conducted Craya–Herring decomposition into the dilatational mode and the solenoidal mode for a compressible Navier–Stokes equation. Then, they showed

https://doi.org/10.1017/jfm.2016.313 Published online by Cambridge University Press

that turbulence is amplified when compressed in a one-dimensional direction. On the other hand, Mahesh, Lele & Moin (1994) conducted RDT numerically for Cartesian coordinates. However, they did not find the analytical solution of RDT. Further, they did not obtain significant changes in the turbulence characteristic length scales.

In this study, we investigate the changes in TKE, enstrophy and turbulence characteristic lengths, and show that the amplifications of the TKE and enstrophy depend on the initial degree of anisotropy. Furthermore, we attempt to answer the unsolved questions in the report by Andreopoulos *et al.* (2000) within the linear theoretical framework.

2. Rapid distortion theory

2.1. *Basic equations*

The starting point of this study is the continuity and momentum equations in a compressible fluid without any gravity effects:

$$\frac{\partial}{\partial t}\rho + \frac{\partial}{\partial x_i}(\rho v_i) = 0, \tag{2.1}$$

$$\rho\frac{\partial}{\partial t}v_i + \rho v_j\frac{\partial}{\partial x_j}v_i = -\frac{\partial p}{\partial x_i} + \frac{\partial}{\partial x_i}\zeta\ \mathrm{div}\ \boldsymbol{v} + \frac{\partial}{\partial x_j}\mu\left(\frac{\partial v_i}{\partial x_j} + \frac{\partial v_j}{\partial x_i}\right), \tag{2.2}$$

where ρ, $\boldsymbol{v}$, p, μ and ζ are the density, velocity, pressure, first coefficient of viscosity and second coefficient of viscosity (under the Stokes assumption, $\zeta = -(2/3)\mu$) respectively. We now divide the density, velocity and pressure fields into mean and fluctuating components, i.e. $v_i = U_i + u_i$, $\rho = \overline{\rho} + \rho'$ and $p = \overline{p} + p'$, where U_i, $\overline{\rho}$ and $\overline{p}$ are the mean components and u_i, ρ' and p' are the fluctuating components. In the Reynolds averaged equation, we assume $\rho' \ll \overline{\rho}$ and neglect ρ' when $\overline{\rho}$ exists, and the density is linearized. This preserves the triad resonant condition in Fourier space, as seen in incompressible turbulence (Marion, Bertoglio & Mathieu 1988).

2.1.1. *Mean flow*

In a compressible flow, the homogeneity requires that the mean flow gradients and mean pressure be spatially uniform; in an incompressible flow, the mean pressure need not be uniform (Durbin & Zeman 1992). In the former case, the requirement of a uniform mean velocity gradient indicates that $\boldsymbol{U}$ is expressed as $\boldsymbol{U} = \boldsymbol{x}\cdot\boldsymbol{S}(t)$, and that of a uniform pressure shows that the velocity satisfies $\mathrm{D}\boldsymbol{U}/\mathrm{D}t = 0$ by substituting the Euler equation, because in turbulence–shock-wave interactions, the mean field satisfies the Rankine–Hugoniot relation. From the continuity equation, the mean density and the adiabatic sound speed are given by

$$\overline{\rho} = \rho_0\,\mathrm{Det}(\boldsymbol{J}), \quad \overline{c^2} = c_0^2[\mathrm{Det}(\boldsymbol{J})]^{\kappa-1}, \tag{2.3a,b}$$

where the subscript 0 indicates the initial state and κ is the ratio of specific heats. The matrix $\boldsymbol{J}$ is given by

$$\boldsymbol{J} = \begin{bmatrix} \dfrac{1}{1+S_1t} & 0 & 0 \\ 0 & \dfrac{1}{1+S_2t} & 0 \\ 0 & 0 & \dfrac{1}{1+S_3t} \end{bmatrix}, \tag{2.4}$$

where S_i is an arbitrary constant. In phenomena such as turbulence–shock-wave interactions, the turbulence is assumed to be strongly compressed in a one-dimensional

https://doi.org/10.1017/jfm.2016.313 Published online by Cambridge University Press

direction, as confirmed by experiments (e.g. Honkan & Andreopoulos 1992; Agui *et al.* 2005) and DNS (e.g. Lee *et al.* 1993; Larsson & Lele 2009). For one-dimensional compression, S_1 is negative and $S_2 = S_3 = 0$. Here, the magnitude of S_1 is the strength of compression. In RDT analysis, the shock-induced compression is approximated as a homogeneous compression. The mean density, determined by continuity, the mean pressure, determined by the isentropic formula, and the adiabatic sound speed are given respectively by

$$\overline{\rho}(t) = \rho_0 \frac{1}{1 + S_1 t}, \quad \overline{p}(t) = p_0 \frac{1}{(1 + S_1 t)^{\kappa}}, \quad \overline{c^2}(t) = c_0^2 \frac{1}{(1 + S_1 t)^{\kappa - 1}}. \tag{2.5a–c}$$

Using the ideal gas law, the kinematic viscosity $\nu(t)$ is given by

$$\nu(t) = \frac{\overline{\mu}}{\overline{\rho}} = \frac{\mu_0}{\overline{\rho}} \left(\frac{\overline{T}}{T_0} \right)^n = \frac{\nu_0}{(1 + S_1 t)^{n(\kappa - 1) - 1}}, \tag{2.6}$$

where the viscosity is given by the power law of temperature T, and the exponent n is taken to be $3/4$, as in Larsson & Lele (2009) and Grube *et al.* (2011). Here, κ is taken to be $\kappa = 7/5$.

2.1.2. *Fluctuations*

Due to the assumption that the mean density is spatially uniform, and given that $\mathrm{D}\boldsymbol{U}/\mathrm{D}t = 0$ and $\mathrm{D}\overline{\rho}/\mathrm{D}t = -\overline{\rho} \nabla \cdot \boldsymbol{U}$, the linearized continuity and momentum equations are given by

$$\frac{\mathrm{D}}{\mathrm{D}t} \left(\frac{p'}{\kappa \overline{p}(t)} \right) = -\mathrm{div}\, \boldsymbol{u}, \tag{2.7}$$

$$\frac{\partial}{\partial t} u_i + U_j \frac{\partial u_i}{\partial x_j} + u_j \frac{\partial U_i}{\partial x_j} = -\overline{c^2}(t) \frac{\partial}{\partial x_i} \left(\frac{p'}{\kappa \overline{p}(t)} \right) + \nu \frac{\partial^2 u_i}{\partial x_j \partial x_j} + \frac{\nu}{3} \frac{\partial}{\partial x_i} \mathrm{div}\, \boldsymbol{u}. \tag{2.8}$$

Here, the conservation of entropy is used. It should be noted that the assumption $\rho' \ll \overline{\rho}$ requires a turbulent Mach number $M_t \ll 1$; this requirement is satisfied when the initial velocity fields consist only of solenoidal modes. Using the Helmholtz decomposition, the velocity fields can be split into irrotational and rotational components,

$$\boldsymbol{u} = \nabla \phi + \nabla \times \boldsymbol{a} = \boldsymbol{u}^d + \boldsymbol{u}^s, \tag{2.9}$$

where ϕ is the scalar potential and $\boldsymbol{a}$ is the vector potential. It should be noted that the dilatational component $\boldsymbol{u}^d$ is irrotational, i.e. $\nabla \times \boldsymbol{u}^d = 0$, and that the solenoidal component $\boldsymbol{u}^s$ satisfies $\nabla \cdot \boldsymbol{u}^s = 0$. Turbulence fluctuations are represented as the superposition of plane waves using Fourier transforms,

$$u_i(\boldsymbol{x}, t) = \int \mathrm{d}\boldsymbol{\chi}\, \hat{u}_i(\boldsymbol{\chi}, t) \exp(\iota \boldsymbol{\chi} \cdot \boldsymbol{x}), \tag{2.10}$$

$$p(\boldsymbol{x}, t) = \int \mathrm{d}\boldsymbol{\chi}\, \hat{p}(\boldsymbol{\chi}, t) \exp(\iota \boldsymbol{\chi} \cdot \boldsymbol{x}), \tag{2.11}$$

where $\boldsymbol{\chi}$ is the wavenumber vector and $\iota = \sqrt{-1}$. Because the system under consideration is treated as homogeneous turbulence, the wavenumber vectors vary in time as follows:

$$\frac{\mathrm{d}\chi_i}{\mathrm{d}t} = -\frac{\partial U_j}{\partial x_i} \chi_j = -S_{ji} \chi_j. \tag{2.12}$$

https://doi.org/10.1017/jfm.2016.313 Published online by Cambridge University Press

Taking the Fourier transform of (2.7) and (2.8) and using (2.12), we obtain

$$\frac{\mathrm{d}}{\mathrm{d}t}\frac{\hat{p}(\boldsymbol{\chi},t)}{\kappa\overline{p}(t)} = -\imath\,\chi\hat{u}^d(\boldsymbol{\chi},t), \tag{2.13}$$

$$\left(\frac{\mathrm{d}}{\mathrm{d}t}+\nu\chi^2\right)\hat{u}_j(\boldsymbol{\chi},t) = -S_{jn}(t)\hat{u}_n(\boldsymbol{\chi},t) - \imath\overline{c^2}(t)\chi_j\frac{\hat{p}(\boldsymbol{\chi},t)}{\kappa\overline{p}(t)} - \frac{\nu}{3}\chi_j\chi_n\hat{u}_n(\boldsymbol{\chi},t). \tag{2.14}$$

It is convenient to introduce two projectors, $\Pi_{ij}(\boldsymbol{\chi})$ and $P_{ij}(\boldsymbol{\chi},t)$, which are expressions in Fourier space of the velocity field against (2.9),

$$\Pi_{ij}(\boldsymbol{\chi}) = \frac{\chi_i\chi_j}{\chi^2}, \quad P_{ij}(\boldsymbol{\chi}) = \delta_{ij} - \frac{\chi_i\chi_j}{\chi^2}, \tag{2.15a,b}$$

where δ_{ij} is the Kronecker delta. Using these projectors, the velocity field can be split into dilatational and solenoidal parts,

$$\hat{u}_i(\boldsymbol{\chi},t) = \hat{u}_i^d(\boldsymbol{\chi},t) + \hat{u}_i^s(\boldsymbol{\chi},t) = \Pi_{ij}(\boldsymbol{\chi})\hat{u}_j(\boldsymbol{\chi},t) + P_{ij}(\boldsymbol{\chi},t)\hat{u}_j(\boldsymbol{\chi},t), \tag{2.16}$$

and using (2.16), it is obvious that the solenoidal mode satisfies

$$\boldsymbol{\chi}\cdot\boldsymbol{u}^s(\boldsymbol{\chi},t) = 0. \tag{2.17}$$

We then consider the evolution of the dilatational and solenoidal modes. Multiplying χ_i by (2.14) and dividing by χ, we obtain

$$\begin{aligned}\left(\frac{\mathrm{d}}{\mathrm{d}t}+\frac{4}{3}\nu(t)\chi^2\right)\hat{u}^d(\boldsymbol{\chi},t) \;=\; & -S_{ij}(t)\Pi_{ij}(\boldsymbol{\chi})\hat{u}^d(\boldsymbol{\chi},t) - 2S_{ij}\frac{\chi_i}{\chi}P_{jn}(\boldsymbol{\chi},t)\hat{u}_n^s(\boldsymbol{\chi},t)\\ & -\imath\,\chi c^2(t)\frac{\hat{p}(\boldsymbol{\chi},t)}{\kappa\overline{p}(t)},\end{aligned} \tag{2.18}$$

where $\hat{u}^d(\boldsymbol{\chi},t) = \chi_j/\chi\,\hat{u}_j^d(\boldsymbol{\chi},t)$. Multiplying $\chi^2 P_{ij}(\boldsymbol{\chi})$ by (2.14) and dividing by χ^2, we obtain

$$\begin{aligned}\left(\frac{\mathrm{d}}{\mathrm{d}t}+\nu(t)\chi^2\right)\hat{u}_i^s(\boldsymbol{\chi},t) \;=\; & \frac{\chi_l}{\chi}P_{ij}(\boldsymbol{\chi})[S_{lj}(t)-S_{jl}(t)]\hat{u}^d(\boldsymbol{\chi},t)\\ & +\left(\frac{\chi_i\chi_l S_{lj}(t)\delta_{jn}}{\chi^2} - P_{ij}(\boldsymbol{\chi})S_{jn}(t)\right)\hat{u}_n^s(\boldsymbol{\chi},t).\end{aligned} \tag{2.19}$$

It should be noted that there is a slight difference in the viscous terms in (2.18) and (2.19). Equations (2.18) and (2.19) are the same as the basis equations of Marion *et al.* (1988) for $S_1 = 0$. The solution to (2.12) can be easily obtained by means of separation of variables. The wavenumber vector $\boldsymbol{\chi}(t)$ is given by

$$\boldsymbol{\chi} = [\chi_1(t),\,\chi_2(t),\,\chi_3(t)] = \left[\frac{k_1}{1+S_1t},\,k_2,\,k_3\right], \tag{2.20}$$

where $\boldsymbol{k} = [k_1,\,k_2,\,k_3]$ is an initial wavenumber vector and $\chi^2 = 1/(1+S_1t)^2[k_1^2 + k_{23}^2(1+S_1t)^2]$, where $k_{23}^2 = k_2^2 + k_3^2$.

2.2. *Rapid distortion theory assumptions for the turbulence–shock-wave interaction*

Rapid distortion theory is a method for solving linearized governing equations under rapid deformation using a statistical technique; RDT solutions are exact solutions of

https://doi.org/10.1017/jfm.2016.313 Published online by Cambridge University Press

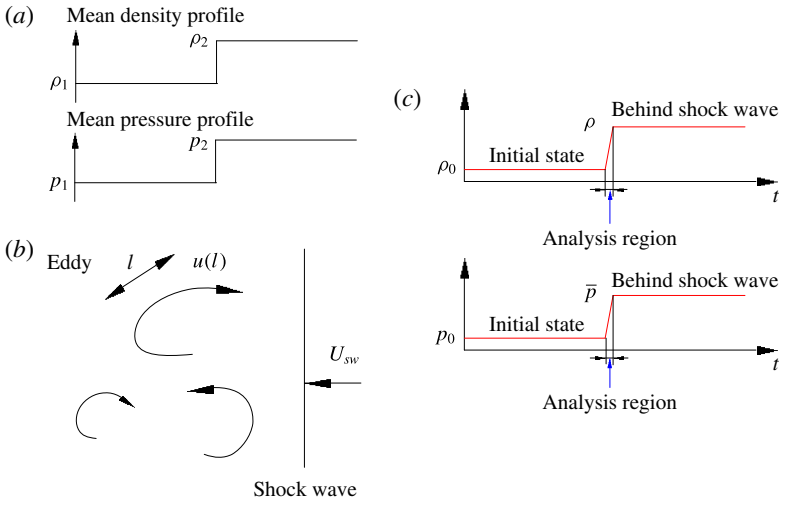


FIGURE 1. (Colour online) (*a*) Mean density and pressure profiles via the Rankine–Hugoniot relation, where the subscript 1 denotes the front of the planar shock wave and the subscript 2 denotes the back of the planar shock wave. (*b*) Schematic of the interaction between turbulence and a shock wave. (*c*) Schematic of the RDT analysis region.

the Navier–Stokes equations if the initial flow is a single plane wave, because the nonlinear terms are exactly zero throughout the triad interaction (Craik & Criminale 1986; Kevlahan & Hunt 1997). Rapid distortion theory equations are obtained by neglecting the nonlinear terms in (2.18) and (2.19) which linearize the equations; this allows analytical solutions for a number of cases. The details of RDT can be found in Hunt & Carruthers (1990), Hunt & Kevlahan (1993) and Kevlahan & Hunt (1997).

Figure 1 shows a schematic of the turbulence–shock-wave interaction. The time scale of the turbulence–shock-wave interaction, T_{SW}, is found to be small relative to the turbulence characteristic time scale, $\tau(l) \sim l/u(l)$, where l is the turbulence characteristic length scale and $u(l)$ is a turbulence characteristic velocity. In addition, if the linear effects of the compression (e.g. $\sim|S_1|(u(l)/l)$ for a compressing distortion) on the vorticity $\boldsymbol{\omega}$ are much stronger than the nonlinear self-induced compression by the turbulence ($\sim(u(l)/l)^2$), the nonlinear terms do not play an important role. When turbulence is compressed by a planar shock wave, the strength of the characteristic compression can be given by

$$|S_1| = \frac{U_{SW} - u_0}{\delta_{SW}}, \tag{2.21}$$

where δ_{SW} is the thickness of the region influenced by the shock-induced compression, U_{SW} is the speed of the shock wave and u_0 is the mean velocity in front of the shock. Thus, the following relations are assumed for the interaction between turbulence and a shock wave:

$$T_{SW} \ll \tau(l) \sim \frac{l}{u(l)} \quad \text{or} \quad |S_1| \gg \frac{u(l)}{l}. \tag{2.22a,b}$$

Equation (2.22*a*) is valid for small values of T_{SW}, whereas (2.22*b*) is valid for large values of $|S_1|$. An overall criterion for the validity of RDT for calculating the statistics of the energy-containing eddies in a given turbulent flow can be derived from (2.22)

https://doi.org/10.1017/jfm.2016.313 Published online by Cambridge University Press

in terms of the r.m.s. velocity u_0 and the integral length scale L (Kevlahan & Hunt 1997). This leads to

$$T_{SW} \ll T_L \sim \frac{L}{u_0} \quad \text{or} \quad \frac{u_0}{L}\frac{1}{|S_1|} \equiv \delta \ll 1, \tag{2.23a,b}$$

where T_L is the integral time scale. This can be re-expressed as

$$\frac{1}{T_L} \ll \max\left(|S_1|, \frac{1}{T_{SW}}\right). \tag{2.24}$$

This criterion should be valid at the start of the distortion. In the present RDT analysis, the deformation of the shock wave is ignored. Kevlahan (1997) showed that the vorticity jump is connected with the shock curvature, the baroclinic effect and the conservation of angular momentum. In RDT analysis, vorticity amplification is interpreted as being caused by the angular momentum created by compression of the flow in the direction normal to the shock wavefront. Therefore, one must note that the present analysis is limited to the case in which the deformation of the shock wave can be ignored. Based on DNS results (Lee *et al.* 1993; Larsson *et al.* 2013), the deformation of a shock wave is slight for $M_t/(M_s - 1) \ll 1$, and therefore RDT is valid for $M_t/(M_s - 1) \ll 1$. The bases of the inviscid RDT equations are (2.13),

$$\frac{\mathrm{d}}{\mathrm{d}t}\hat{u}^d(\boldsymbol{\chi}, t) = -S_{ij}(t)\Pi_{ij}(\boldsymbol{\chi})\hat{u}^d(\boldsymbol{\chi}, t) - 2S_{ij}\frac{\chi_i}{\chi}P_{jn}(\boldsymbol{\chi}, t)\hat{u}^s_n(\boldsymbol{\chi}, t) - \imath\chi c^2(t)\frac{\hat{p}(\boldsymbol{\chi}, t)}{\kappa\overline{p}(t)}, \tag{2.25}$$

$$\frac{\mathrm{d}}{\mathrm{d}t}\hat{u}^s_i(\boldsymbol{\chi}, t) = \frac{\chi_l}{\chi}P_{ij}(\boldsymbol{\chi})[S_{lj}(t) - S_{jl}(t)]\hat{u}^d(\boldsymbol{\chi}, t) + \left(\frac{\chi_i\chi_l S_{lj}(t)\delta_{jn}}{\chi^2} - P_{ij}(\boldsymbol{\chi})S_{jn}(t)\right)\hat{u}^s_n(\boldsymbol{\chi}, t). \tag{2.26}$$

It should be noted that the dilatational mode in (2.26) disappears because of the symmetrical form of $S_{lj}(t) = \delta_{l1}S_{11}(t)\delta_{j1}$. For one-dimensional compression, (2.26) is the same as in Mahesh *et al.* (1994) without shear. However, these authors did not obtain the analytical solutions and only performed a numerical analysis. The solutions to the system are expected to have the form

$$\hat{u}^s_i(\boldsymbol{\chi}, t) = G^s_{ij}(\boldsymbol{\chi}, t)\hat{u}^s_j(\boldsymbol{k}, 0), \tag{2.27}$$

$$\hat{u}^d_i(\boldsymbol{\chi}, t) = G^d_{ij}(\boldsymbol{\chi}, t)\hat{u}_j(\boldsymbol{k}, 0) + G^p(\boldsymbol{\chi}, t)\hat{p}(\boldsymbol{k}, 0), \tag{2.28}$$

where $\boldsymbol{G}$ are Green functions.

2.3. *Ordinary differential equations and analytical solution for inviscid RDT*

We consider the analytical solution of the inviscid RDT equations. From (2.26) and the solenoidal condition (2.17), we obtain

$$\underbrace{\frac{\mathrm{d}}{\mathrm{d}t}\begin{bmatrix}\hat{u}^s_1(\boldsymbol{\chi}, t)\\ \hat{u}^s_2(\boldsymbol{\chi}, t)\\ \hat{u}^s_3(\boldsymbol{\chi}, t)\end{bmatrix}}_{\dot{\hat{\boldsymbol{u}}}^s} = \underbrace{\frac{S_1}{k_1^2 + k_{23}^2(1 + S_1t)^2}\begin{bmatrix}-k_{23}^2(1 + S_1t) & -k_1k_2 & -k_1k_3\\ k_1k_2 & -k_2^2(1 + S_1t) & -k_2k_3(1 + S_1t)\\ k_1k_3 & -k_2k_3(1 + S_1t) & -k_3^2(1 + S_1t)\end{bmatrix}}_{\boldsymbol{A}} \times \underbrace{\begin{bmatrix}\hat{u}^s_1(\boldsymbol{\chi}, t)\\ \hat{u}^s_2(\boldsymbol{\chi}, t)\\ \hat{u}^s_3(\boldsymbol{\chi}, t)\end{bmatrix}}_{\hat{\boldsymbol{u}}^s}. \tag{2.29}$$

https://doi.org/10.1017/jfm.2016.313 Published online by Cambridge University Press

Here, the method for solving the ordinary differential equations (ODEs) is described briefly, because cumbersome calculations are required to solve them analytically (see appendix A for details). The ODE will be set to $(\mathrm{d}\hat{u}_i^s(\boldsymbol{\chi}, t))/\mathrm{d}t = A_{ij}(t)\hat{u}_j^s(\boldsymbol{\chi}, t)$ if the tensor notation of (2.29) is utilized. We then determine the eigenvalues of $A_{ij}(t)$. After some algebra, the eigenvalues of $A_{ij}(t)$ are as follows:

$$\lambda = 0, -\frac{S_1 k_{23}^2(1+S_1 t) + \imath S_1 k_1 k_{23}}{k_1^2 + k_{23}^2(1+S_1 t)^2}, -\frac{S_1 k_{23}^2(1+S_1 t) - \imath S_1 k_1 k_{23}}{k_1^2 + k_{23}^2(1+S_1 t)^2}. \tag{2.30}$$

Each eigenvector can be obtained for the acquired eigenvalues. Let B_{ij} be the transformation matrix which consists of eigenvectors. A diagonal matrix $D_{\alpha\beta}(t)$ can be expressed as $D_{\alpha\beta}(t) = B_{\alpha i}^{-1} A_{ij}(t) B_{j\beta}$. Multiplying B_{ij}^{-1} to (2.29) from the left side, we obtain $(\mathrm{d}y_i(\boldsymbol{\chi}, t))/\mathrm{d}t = D_{ij}(t) y_j(\boldsymbol{\chi}, t)$, where $y_i(\boldsymbol{\chi}, t) = B_{ij}^{-1}\hat{u}_i^s(\boldsymbol{\chi}, t)$. Because $D_{ij}(t)$ is a symmetrical tensor, which has only diagonal components, the solution to $y_i(\boldsymbol{\chi}, t)$ is obtained using separation of variables. If the relationship $\hat{u}_i^s(\boldsymbol{\chi}, t) = B_{ij} y_j(\boldsymbol{\chi}, t)$ and the initial conditions $y_i(\boldsymbol{k}, 0) = B_{ij}\hat{u}_j^s(\boldsymbol{k}, 0)$ are used, analytical solutions are given by

$$\begin{aligned}\hat{u}_1^s(\boldsymbol{\chi}, t) &= P\hat{u}_1^s(\boldsymbol{k}, 0) - \frac{k_2 Q}{k_{23}}\hat{u}_2^s(\boldsymbol{k}, 0) - \frac{k_3 Q}{k_{23}}\hat{u}_3^s(\boldsymbol{k}, 0) \\ &= \frac{k^2(1+S_1 t)}{k_1^2 + k_{23}^2(1+S_1 t)^2}\hat{u}_1^s(\boldsymbol{k}, 0),\end{aligned} \tag{2.31}$$

$$\begin{aligned}\hat{u}_2^s(\boldsymbol{\chi}, t) &= \frac{k_2 Q}{k_{23}}\hat{u}_1^s(\boldsymbol{k}, 0) + \frac{k_3^2 + k_2^2 P}{k_{23}^2}\hat{u}_2^s(\boldsymbol{k}, 0) + \frac{k_2 k_3}{k_{23}^2}(P-1)\hat{u}_3^s(\boldsymbol{k}, 0) \\ &= \frac{k_1 k_2 S_1 t(2+S_1 t)}{k_1^2 + k_{23}^2(1+S_1 t)^2}\hat{u}_1^s(\boldsymbol{k}, 0) + \hat{u}_2^s(\boldsymbol{k}, 0),\end{aligned} \tag{2.32}$$

$$\begin{aligned}\hat{u}_3^s(\boldsymbol{\chi}, t) &= \frac{k_3 Q}{k_{23}}\hat{u}_1^s(\boldsymbol{k}, 0) + \frac{k_2 k_3}{k_{23}^2}(P-1)\hat{u}_2^s(\boldsymbol{k}, 0) + \frac{k_2^2 + k_3^2 P}{k_{23}^2}\hat{u}_3^s(\boldsymbol{k}, 0) \\ &= \frac{k_1 k_3 S_1 t(2+S_1 t)}{k_1^2 + k_{23}^2(1+S_1 t)^2}\hat{u}_1^s(\boldsymbol{k}, 0) + \hat{u}_3^s(\boldsymbol{k}, 0),\end{aligned} \tag{2.33}$$

where

$$P = \frac{k_1^2 + k_{23}^2(1+S_1 t)}{k_1^2 + k_{23}^2(1+S_1 t)^2}, \tag{2.34}$$

$$Q = \frac{k_1 k_{23} S_1 t}{k_1^2 + k_{23}^2(1+S_1 t)^2}. \tag{2.35}$$

For convenience in later discussions, the analytical solutions in the Craya–Herring decomposition are given by

$$\hat{u}^{(1)}(\boldsymbol{\chi}, t) = \frac{\imath}{k_{23}}\hat{\omega}_1^s(\boldsymbol{\chi}, t) = \left[\frac{k_3}{k_{23}}\hat{u}_2^s(\boldsymbol{k}, 0) - \frac{k_2}{k_{23}}\hat{u}_3^s(\boldsymbol{k}, 0)\right], \tag{2.36}$$

$$\hat{u}^{(2)}(\boldsymbol{\chi}, t) = -\frac{\chi}{\chi_{23}}\hat{u}_1^s(\boldsymbol{\chi}, t) = -\frac{k^2}{k_{23}}\frac{\hat{u}_1^s(\boldsymbol{k}, 0)}{\sqrt{k_1^2 + k_{23}^2(1+S_1 t)^2}}. \tag{2.37}$$

Interestingly, the vortex mode, $\hat{u}^{(1)}(\boldsymbol{\chi}, t)$, is not affected by the rapid one-dimensional compression, whereas the wave mode, $\hat{u}^{(2)}(\boldsymbol{\chi}, t)$, is strongly affected. Thus, the

https://doi.org/10.1017/jfm.2016.313 Published online by Cambridge University Press

vorticity in the one-dimensional compressed direction does not change throughout the turbulence–shock-wave interaction in the limiting case, as discussed later. This situation is similar to that in stratified turbulence (Hanazaki & Hunt 1996). The fact that the vorticity does not change in the compressed direction is a direct result of the jump conditions for vorticity. Kevlahan (1997) also showed that the vorticity only increases in the plane tangent to a shock wave.

After some algebra, the inviscid RDT equation for the dilatational mode becomes

$$\frac{\mathrm{d}}{\mathrm{d}t}\left[\frac{(1+S_1t)^{\kappa+1}}{k_1^2+k_{23}^2(1+S_1t)^2}\frac{\mathrm{d}\hat{u}^d(\boldsymbol{\chi},t)}{\mathrm{d}t}\right]+\frac{(1+S_1t)^{\kappa+1}}{k_1^2+k_{23}^2(1+S_1t)^2}\chi c^2(t)R(t)\hat{u}^d(t)$$
$$=-\frac{(1+S_1t)^{\kappa+1}}{k_1^2+k_{23}^2(1+S_1t)^2}\chi c^2(t)\frac{\mathrm{d}}{\mathrm{d}t}\left(\frac{2S_1k^2k_1(1+S_1t)^{\kappa}}{c_0^2[k_1^2+k_{23}^2(1+S_1t)^2]^2}\right)\hat{u}_1^s(\boldsymbol{k},0), \quad (2.38)$$

where $R(t)$ is given by

$$R(t)=\frac{\mathrm{d}}{\mathrm{d}t}\left(\frac{S_{11}(t)\Pi_{11}(\boldsymbol{\chi})}{\chi c^2(t)}\right)+\chi, \quad (2.39)$$

and the left-hand side of (2.38) is a typical Sturm–Liouville equation. Thus, the analytical solution is assumed to be a special function such as a Legendre function (e.g. Hanazaki & Hunt 2004). In general, the analytical solution will take the form $\hat{u}^d(\boldsymbol{\chi},t)=u_0(t)+C_1u_1(t)+C_1u_2(t)$, where u_0 is a particular solution, and $u_1(t)$ and $u_2(t)$ are basis solutions. If one basis solution is found, the analytical solution of the dilatational mode can be obtained. When $S_1=0$, the analytical solutions are expressed by trigonometric functions (Marion *et al.* 1988). Unfortunately, we could not find any analytical solutions for the dilatational mode. Thus, hereinafter we only discuss the RDT solutions of the solenoidal mode. It should be noted that Jacquin *et al.* (1993) found the analytical solution for the case in which the second term of (2.38) is neglected.

3. Homogeneous axisymmetric turbulence

Homogeneous axisymmetrical tensors in Cartesian coordinates have been developed by Batchelor (1946, 1953) and Chandrasekhar (1950). The general second-order two-point correlation has the form

$$\Phi_{ij}(\boldsymbol{k})=A_1k_ik_j+A_2n_in_j+A_3\delta_{ij}+A_4n_ik_j+A_5n_jk_i, \quad (3.1)$$

where $A_1\sim A_5$ are functions (not all independent) of k^2 and $k\cos\theta=\boldsymbol{k}\cdot\boldsymbol{n}$, where $\boldsymbol{n}$ is a unit vector in the direction of the symmetry axis.

We obtain the relation $A_4=A_5$ from the reflection invariant, $\Phi_{ij}(\boldsymbol{k})=\Phi_{ij}(-\boldsymbol{k})$, which implies the symmetry condition $\Phi_{ij}(\boldsymbol{k})=\Phi_{ji}(\boldsymbol{k})$. Then, we obtain the following relation from the solenoidal condition $k_i\Phi_{ij}(\boldsymbol{k})=k_j\Phi_{ij}(\boldsymbol{k})=0$:

$$\Phi_{ij}(\boldsymbol{k})=-k^2P_{ij}(\boldsymbol{k})A_1(k,\cos\theta)+H_{ij}(\boldsymbol{k})A_2(k,\cos\theta), \quad (3.2)$$

$$H_{ij}(\boldsymbol{k})=n_in_j+\frac{(\boldsymbol{k}\cdot\boldsymbol{n})^2}{k^2}\delta_{ij}-(\boldsymbol{k}\cdot\boldsymbol{n})\frac{n_ik_j+n_jk_i}{k^2}=\cos^2\theta e_i^{(1)}(\boldsymbol{k})e_j^{(1)}(\boldsymbol{k})+e_i^{(2)}(\boldsymbol{k})e_j^{(2)}(\boldsymbol{k}), \quad (3.3)$$

https://doi.org/10.1017/jfm.2016.313 Published online by Cambridge University Press

where $\boldsymbol{e}^{(1)}(\boldsymbol{\chi})$ and $\boldsymbol{e}^{(2)}(\boldsymbol{\chi})$ are the basis unit vectors of the Craya–Herring decomposition, defined as

$$\boldsymbol{e}^{(1)}(\boldsymbol{\chi}) = \frac{\boldsymbol{\chi} \times \boldsymbol{n}}{|\boldsymbol{\chi} \times \boldsymbol{n}|}, \quad \boldsymbol{e}^{(2)}(\boldsymbol{\chi}) = \frac{\boldsymbol{\chi}}{\chi} \times \boldsymbol{e}^{(1)}(\boldsymbol{\chi}). \tag{3.4a,b}$$

For homogeneous isotropic turbulence, $A_1(k, \cos\theta) = -E(k)/4\pi k^4$ and $A_2(k, \cos\theta) = 0$ are satisfied. In the Craya–Herring frame, $\Phi_{ij}(\boldsymbol{\chi}, t)$ is given by

$$\Phi_{ij}(\boldsymbol{k}) = e_i^{(1)}(\boldsymbol{k}) e_j^{(1)}(\boldsymbol{k}) \underbrace{[-k^2 A_1(\boldsymbol{k}) + \cos^2\theta A_2(\boldsymbol{k})]}_{Q^{(1)}(\boldsymbol{k})} + e_i^{(2)}(\boldsymbol{k}) e_j^{(2)}(\boldsymbol{k}) \underbrace{[-k^2 A_1(\boldsymbol{k}) + A_2(\boldsymbol{k})]}_{Q^{(2)}(\boldsymbol{k})}. \tag{3.5}$$

From the obtained analytical solutions (2.31)–(2.33), the energy spectral tensors are given by

$$\Phi_{\parallel}(\boldsymbol{\chi}, t) = \Phi_{11}(\boldsymbol{\chi}, t) = Q^{(2)}(\boldsymbol{k}, 0) \frac{k^2 k_{23}^2 (1 + S_1 t)^2}{[k_1^2 + k_{23}^2 (1 + S_1 t)^2]^2}, \tag{3.6}$$

$$\Phi_{22}(\boldsymbol{\chi}, t) = \frac{k_3^2}{k_{23}^2} Q^{(1)}(\boldsymbol{k}, 0) + \frac{Q^{(2)}(\boldsymbol{k}, 0) k_2^2}{k^2} \left(\frac{k_1^2}{k_{23}^2} P^2 + Q^2 - 2 \frac{k_1}{k_{23}} PQ \right), \tag{3.7}$$

$$\Phi_{33}(\boldsymbol{\chi}, t) = \frac{k_2^2}{k_{23}^2} Q^{(1)}(\boldsymbol{k}, 0) + \frac{Q^{(2)}(\boldsymbol{k}, 0) k_3^2}{k^2} \left(\frac{k_1^2}{k_{23}^2} P^2 + Q^2 - 2 \frac{k_1}{k_{23}} PQ \right), \tag{3.8}$$

$$\begin{aligned} \Phi_{\perp}(\boldsymbol{\chi}, t) &= \frac{1}{2} [\Phi_{22}(\boldsymbol{\chi}, t) + \Phi_{33}(\boldsymbol{\chi}, t)] \\ &= \frac{1}{2} \left[Q^{(1)}(\boldsymbol{k}, 0) + Q^{(2)}(\boldsymbol{k}, 0) \frac{k^2 k_1^2}{[k_1^2 + k_{23}^2 (1 + S_1 t)^2]^2} \right], \end{aligned} \tag{3.9}$$

$$\Phi_{ii}(\boldsymbol{\chi}, t) = \Phi_{\parallel}(\boldsymbol{\chi}, t) + 2\Phi_{\perp}(\boldsymbol{\chi}, t) = Q^{(1)}(\boldsymbol{k}, 0) + Q^{(2)}(\boldsymbol{k}, 0)(P^2 + Q^2), \tag{3.10}$$

where $Q^{(1)}(\boldsymbol{k}, 0) = Q^{(11)}(\boldsymbol{k}, 0)$ and $Q^{(2)}(\boldsymbol{k}, 0) = Q^{(22)}(\boldsymbol{k}, 0)$ for simplicity, and $Q^{(1)}(\boldsymbol{k}, 0) = Q^{(2)}(\boldsymbol{k}, 0) = (E(k, 0))/4\pi k^2$ when the initial turbulence is homogeneous isotropic turbulence, where $E(k, 0)$ is the energy spectrum. It should be noted that the energy spectral tensor in the compressed direction, $\Phi_{11}(\boldsymbol{\chi}, t)$, is related only to the wave mode, $Q^{(2)}(\boldsymbol{k})$; it is not related to the vortex mode, $Q^{(1)}(\boldsymbol{k})$. Therefore, we can interpret the change in variance of u_1 as a direct consequence of the initial distribution of the wave mode, with no dependence on the initial vortex mode. Thus, the obtained results depend on the initial complexity of the energy distribution.

In homogeneous turbulence, we have the following relation between the energy spectral tensor, $\Phi_{ij}(\boldsymbol{\chi}, t)$, and the enstrophy spectral tensor, $\Omega_{ij}(\boldsymbol{\chi}, t)$ (Batchelor 1953):

$$\Omega_{ij}(\boldsymbol{\chi}, t) = \langle \hat{\omega}_i(\boldsymbol{\chi}, t) \hat{\omega}_j^*(\boldsymbol{\chi}, t) \rangle = \chi^2 P_{ij}(\boldsymbol{\chi}, t) \Phi_{ll}(\boldsymbol{\chi}, t) - \chi^2 \Phi_{ji}(\boldsymbol{\chi}, t). \tag{3.11}$$

Here, $\hat{\omega}_i(\boldsymbol{\chi}, t) = \imath \epsilon_{ijk} \chi_j \hat{u}_k(\boldsymbol{\chi}, t)$, where ϵ_{ijk} is the Levi-Civita symbol. Thus, from the obtained analytical solutions (2.31)–(2.33), the enstrophy spectral tensors are given by

$$\begin{aligned} \Omega_{\parallel}(\boldsymbol{\chi}, t) &= \Omega_{11}(\boldsymbol{\chi}, t) = \langle \hat{\omega}_1(\boldsymbol{\chi}, t) \hat{\omega}_1^*(\boldsymbol{\chi}, t) \rangle \\ &= \Omega_{11}(\boldsymbol{k}, 0) = k_{23}^2 Q^{(1)}(\boldsymbol{k}, 0), \end{aligned} \tag{3.12}$$

https://doi.org/10.1017/jfm.2016.313 Published online by Cambridge University Press

$$\Omega_{\perp}(\boldsymbol{\chi}, t) = \frac{1}{2}[\Omega_{22}(\boldsymbol{\chi}, t) + \Omega_{33}(\boldsymbol{\chi}, t)]$$
$$= \frac{1}{2}\left[\frac{k_1^2}{(1+S_1t)^2}Q^{(1)}(\boldsymbol{k}, 0) + \frac{k_1^2 + k_{23}^2(1+S_1t)^2}{(1+S_1t)^2}Q^{(2)}(\boldsymbol{k}, 0)(P^2+Q^2)\right], \quad (3.13)$$

$$\Omega_{ll}(\boldsymbol{\chi}, t) = \chi^2\Phi_{ll}(\boldsymbol{\chi}, t) = \left[\frac{k_1^2}{(1+S_1t)^2} + k_{23}^2\right]\Phi_{ll}(\boldsymbol{\chi}, t)$$
$$= \frac{k_1^2 + k_{23}^2(1+S_1t)^2}{(1+S_1t)^2}[Q^{(1)}(\boldsymbol{k}, 0) + Q^{(2)}(\boldsymbol{k}, 0)(P^2+Q^2)]. \quad (3.14)$$

As shown in (3.12), it is obvious that the parallel enstrophy spectral tensor is independent of rapid one-dimensional compression.

4. Model spectra

In general, there is no precise analytical expression for experimental turbulent energy spectra. To discuss the Reynolds number dependence for non-zero viscosity and the energy distribution for homogeneous axisymmetric turbulence as an initial state, we used five energy spectra.

4.1. *Model spectra for homogeneous isotropic turbulence (model spectrum A)*

The following model spectrum describes the different forms of energy over a wide range of wavenumbers (Davidson 2004):

$$E(k) = \frac{K_0\epsilon^{2/3}k^{-5/3}}{\left[1 + \frac{3K_0}{2}(kL)^{-2/3}\right]^m}\exp\left[-\frac{3K_0}{2}(k\eta)^{4/3}\right], \quad (4.1)$$

where K_0 corresponds to the Kolmogorov constant, which was set to 1.52 in this study, and m corresponds to the parameter that determines the slope of the energy spectrum at low wavenumbers: $E(k\to 0)\sim k^2$ for $m = 11/2$ and $E(k\to 0)\sim k^4$ for $m = 17/2$. In this study, we adopted a Saffman-type energy spectrum as an initial condition because there is experimental evidence of Saffman turbulence in grid turbulence (Krogstad & Davidson 2010; Kitamura *et al.* 2014). In this study, the model spectrum (4.1) was transformed as a function of Re_λ to investigate the dependence on turbulence of the Reynolds number based on the Taylor microscale for the non-zero-viscosity RDT solutions. Using Taylor–Kolmogorov scaling, $\eta/L \approx 15^{3/4}Re_\lambda^{-3/2}$, the transformed model spectrum is described by

$$E(k) = \frac{K_0\epsilon^{2/3}k^{-5/3}}{\left[1 + \frac{3K_0}{2}(kL)^{-2/3}\right]^{11/2}}\exp[-15K_0\,Re_\lambda^{-2}(kL)^{4/3}]. \quad (4.2)$$

In this study, we investigated the following Re_λ dependences for non-zero-viscosity RDT: (i) $Re_\lambda = 10^2$ and (ii) $Re_\lambda = 10^4$. The turbulent flow at $Re_\lambda = 10^2$ is a typical flow such as grid turbulence, whereas the turbulent flow at $Re_\lambda = 10^4$ is a typical flow such as atmospheric turbulence.

https://doi.org/10.1017/jfm.2016.313 Published online by Cambridge University Press

4.2. *Model spectra for homogeneous axisymmetric turbulence*

Sreenivasan & Narasimha (1978) proposed that a homogeneous axisymmetrical tensor can be described by the expansion in zonal harmonics of the two independent scalar functions. The terms A_1 and A_2 can be expanded in zonal harmonics with the Legendre polynomial $P_{2m}(\cos\theta)$ as a basis function:

$$-k^2A_1(\boldsymbol{k},\theta)+A_2(\boldsymbol{k},\theta)=\sum_{m=0}^{\infty}F_{2m}(\boldsymbol{k})P_{2m}(\cos\theta), \tag{4.3}$$

$$A_2(\boldsymbol{k},\theta)=\sum_{m=0}^{\infty}G_{2m}(\boldsymbol{k})P_{2m}(\cos\theta). \tag{4.4}$$

The expansion in terms of spherical harmonics was generalized by Cambon & Teissèdre (1985) for arbitrary anisotropy. This expansion is consistent with that of Sreenivasan & Narasimha (1978) for axisymmetry.

By postulating that some pair of functions A_i $(i=1,\ldots,4)$ depends only on k and not on $\cos\theta$, and using (4.3) and (4.4), a more concrete form of the energy spectral tensor can be obtained. Sreenivasan & Narasimha (1978) proposed the following three ansatzes for homogeneous axisymmetric turbulence.

(i) Ansatz 1: A_1 and A_2 depend only on k.
(ii) Ansatz 2: A_2 and A_3 depend only on k.
(iii) Ansatz 3: A_1 and A_3 depend only on k.

In these three ansatzes, Ansatz 1 is the simplest model because the angular dependence appears throughout $P_{ij}(\boldsymbol{k})$ and $H_{ij}(\boldsymbol{k})$. Ansatz 2 is the more harmonic form (as compared with Ansatz 1) because it contains higher-order Legendre polynomials, e.g. $F_2(k)P_2(\cos\theta)$. In Ansatz 3, $A_2(k,\cos\theta)$ can be expressed as $A_2(k,\cos\theta)=(1/\cos^2\theta)[A_3-k^2A_1]$, where A_3 and A_1 are functions of k. As mentioned by Sreenivasan & Narasimha (1978), $A_1(k,\cos\theta)$ and $A_2(k,\cos\theta)$ do not depend on the angular dependence when $k^2A_1=-A_3$; therefore, they become isotropic forms. On the other hand, $A_2(k,\cos\theta)$ exhibits singularity for $\cos\theta=0$ when $k^2A_1\neq-A_3$.

From the abovementioned background for the three ansatzes, we used Ansatzes 1 and 2 for the model spectra.

4.2.1. *Model spectra for Ansatz 1 (model spectrum B)*

Ansatz 1 represents what is likely to be the simplest model for anisotropic turbulence (Nagata *et al.* 2006). Because A_1 and A_2 are functions of only k in Ansatz 1, the form of $\Phi_{ij}(\boldsymbol{k})$ is obtained using the following simple relation:

$$F_{2m}(k)=G_{2m}(k)=0,\quad m=1,2,\ldots. \tag{4.5}$$

Thus, the energy spectral tensor is given by

$$\Phi_{ij}(\boldsymbol{k})=P_{ij}(\boldsymbol{k})(F_0(k)-G_0(k))+H_{ij}(\boldsymbol{k})G_0(k)=-k^2P_{ij}(\boldsymbol{k})A_1(k)+H_{ij}(\boldsymbol{k})A_2(k). \tag{4.6}$$

In the expression of the Craya–Herring decomposition, the energy spectral tensor is expressed by

$$\Phi_{ij}(\boldsymbol{k})=\underbrace{[-k^2A_1(k)+\cos^2\theta A_2(k)]}_{Q^{(1)}(\boldsymbol{k})}e_i^{(1)}(\boldsymbol{k})e_j^{(1)}(\boldsymbol{k})+\underbrace{[-k^2A_1(k)+A_2(k)]}_{Q^{(2)}(k)}e_i^{(2)}(\boldsymbol{k})e_j^{(2)}(\boldsymbol{k}). \tag{4.7}$$

https://doi.org/10.1017/jfm.2016.313 Published online by Cambridge University Press

From the restrictions of the real functions of $Q^{(1)}(\boldsymbol{k})$ and $Q^{(2)}(\boldsymbol{k})$, $A_1(k)$ is negative and $-k^2A_1(k)+A_2(k)>0$. In the model spectrum of Nagata *et al.* (2006), the forms of A_1 and A_2 are taken to be the exponential forms

$$A_1=-\mathscr{B}_1\exp(-\mathscr{R}_1k^2),\quad A_2=\mathscr{B}_2k^2\exp(-\mathscr{R}_2k^2), \tag{4.8a,b}$$

where $\mathscr{B}_1$ and $\mathscr{B}_2$ are constants and $1/\mathscr{R}_1^{1/2}$ and $1/\mathscr{R}_2^{1/2}$ are proportional to the length scales of the isotropic and anisotropic components respectively. For isotropic turbulence, $\mathscr{B}_2=0$, $\mathscr{B}_1=1/\pi^4$ and $\mathscr{R}_1=1/\pi$.

To determine the unknown coefficients, Nagata *et al.* (2006) prescribed the strength of the anisotropy

$$\frac{\displaystyle\int \mathrm{d}\boldsymbol{k}\,\Phi_{ii}(\boldsymbol{k})}{\displaystyle\int \mathrm{d}\boldsymbol{k}\,\Phi_{11}(\boldsymbol{k})}=\frac{\langle u_i^2\rangle}{\langle u_1^2\rangle}=\left[1,\frac{1}{R_u},\frac{1}{R_u}\right]\quad\text{(no summation with respect to } i\text{)} \tag{4.9}$$

and the relation of the one-dimensional spectrum $\Theta_{11}(k_1)$ at $k_1=0$ as

$$\Theta_{11}(0)=\frac{u_1^2}{2\pi}\int_{-\infty}^{\infty}\mathrm{d}r\langle u_1(\boldsymbol{x})u_1(\boldsymbol{x}+r\boldsymbol{e}_1)\rangle=\frac{\langle u_1^2\rangle}{\pi}L_{11}. \tag{4.10}$$

The coefficients in (4.8) are given in § B.1, following Nagata *et al.* (2006). It should be noted that R_u is restricted to lie within the range $1\leqslant R_u<2$ so as to satisfy the non-negative Hermitian form of $\Phi_{ij}(\boldsymbol{k})$. When $R_u=2$, the integral length scale $L_{22,1}$ $(=L_{33,1})$ becomes zero, which is unphysical. More detail is given in Nagata *et al.* (2006). The model spectrum of Nagata *et al.* (2006) is for low-Reynolds-number flow, as seen in the grid turbulence. In the model spectrum for high-Reynolds-number flow, the forms of A_1 and A_2 are taken to be of the von Kármán spectral type, as follows:

$$A_1(k)=-\mathscr{B}_1\frac{1}{[1+(\mathscr{R}_1k)^2]^{17/6}},\quad A_2(k)=\mathscr{B}_2\frac{k^2}{[1+(\mathscr{R}_2k)^2]^{17/6}}. \tag{4.11a,b}$$

In a similar way to Nagata *et al.* (2006), the unknown coefficients are obtained and given in § B.2. In the case of inviscid RDT (as described later), there is no dependence of the forms of A_1 and A_2 on the change in TKE. When the von Kármán forms are adopted, the enstrophy is seen to diverge because of the power law form.

4.2.2. *Model spectra for Ansatz 2 (model spectrum C)*

In Ansatz 2, A_2 and A_3 are functions of k. Thus, $G_{2m}(k)=0$ for $m=1,2,\ldots$. In addition, the relation $A_2(k)=G_0(k)=-3/2F_2(k)$ is obtained using $P_2(\cos\theta)=1/2(3\cos^2\theta-1)$. Finally, the following relations are obtained:

$$G_0(k)=-\tfrac{3}{2}F_2(k),\quad F_{2m+2}(k)=0=G_{2m}(k),\quad m=1,2,\ldots. \tag{4.12a,b}$$

Thus, the energy spectral tensor is given by

$$\Phi_{ij}(\boldsymbol{k})=P_{ij}(\boldsymbol{k})F_0(k)+\left[P_{ij}(\boldsymbol{k})\left(\tfrac{3}{2}\cos^2\theta+1\right)-\tfrac{3}{2}H_{ij}(\boldsymbol{k})\right]F_2(k). \tag{4.13}$$

Unlike the form of the energy spectral tensor in Ansatz 1, the angular dependence appears in $A_1(\boldsymbol{k})$. In the expression of the Craya–Herring decomposition, the energy spectral tensor is given by

$$\Phi_{ij}(\boldsymbol{k})=\underbrace{[F_0(k)+F_2(k)]}_{Q^{(1)}(k)}e_i^{(1)}(\boldsymbol{k})e_j^{(1)}(\boldsymbol{k})+\underbrace{\left[F_0(k)+\left(\tfrac{3}{2}\cos^2\theta-\tfrac{1}{2}\right)F_2(k)\right]}_{Q^{(2)}(\boldsymbol{k})}e_i^{(2)}(\boldsymbol{k})e_j^{(2)}(\boldsymbol{k}). \tag{4.14}$$

https://doi.org/10.1017/jfm.2016.313 Published online by Cambridge University Press

From the restriction of the real functions of $Q^{(1)}(\boldsymbol{k})$ and $Q^{(2)}(\boldsymbol{k})$, $F_0(k) + F_2(k) > 0$ and $F_0(k) > (1/2)F_2(k)$. When $F_2(k)$ is negative, $A_2(k)$ is positive. In this case, the magnitude of $F_0(k)$ must be larger than that of $F_2(k)$, regardless of θ.

Similarly to Ansatz 1, the exponential forms for $F_0(k)$ and $F_2(k)$,

$$F_0(k) = \mathscr{F}_0 k^2 \exp(-\mathscr{L}_0 k^2), \quad F_2(k) = \mathscr{F}_2 k^2 \exp(-\mathscr{L}_2 k^2), \tag{4.15a,b}$$

and the von Kármán forms,

$$F_0(k) = \mathscr{F}_0 \frac{k^2}{[1 + (\mathscr{L}_0 k)^2]^{17/6}}, \quad F_2(k) = \mathscr{F}_2 \frac{k^2}{[1 + (\mathscr{L}_2 k)^2]^{17/6}}, \tag{4.16a,b}$$

have been adopted, in which the coefficients $\mathscr{L}_0$, $\mathscr{L}_2$, $\mathscr{F}_0$ and $\mathscr{F}_2$ are determined using a similar method to that used for Ansatz 1; they are given in §§ B.3 and B.4 for the exponential and von Kármán types respectively.

5. Results and discussion for inviscid RDT

5.1. *Angular distribution of the energy spectral tensor*

In homogeneous anisotropic turbulence, there is an angular dependence for $Q^{(1)}(\boldsymbol{\chi}, t)$ and $Q^{(2)}(\boldsymbol{\chi}, t)$. When we discuss the departure from isotropy, it is convenient to introduce the e–z decomposition (Sagaut & Cambon 2008). For instance, the angular dependence of the anisotropic turbulence has been discussed by Cambon, Mansour & Godefeferd (1997). However, in this study, the angular distribution of the parallel and perpendicular energy spectral tensors is discussed to better understand the phenomena in turbulence–shock-wave interactions.

Figures 2 and 3 show the changes in angular dependence of the energy spectral tensors, $\Phi_\parallel(\boldsymbol{\chi}, t)$ and $\Phi_\perp(\boldsymbol{\chi}, t)$, for model spectra A and B respectively. In model spectrum A, the spectral tensor has energy at low wavenumbers, and this is caused by the Saffman form at low wavenumbers, whereas in model spectrum B (and C, not shown), the spectral tensor has energy near the inverse of the integral length scale, and this is due to the Batchelor form at low wavenumbers. When initial isotropic conditions are considered, there is a slight change in the angular distribution of $\Phi_\parallel(\boldsymbol{\chi}, t)$, whereas the energy concentrates to approximately $\theta = \pi/4$ in the angular distribution of $\Phi_\perp(\boldsymbol{\chi}, t)$. As shown in figures 2 and 3, the shock-induced one-dimensional compression (hereinafter simply 'compression') transfers energy to high wavenumbers. This energy transfer was seen in $\Phi_\perp(\boldsymbol{\chi}, t)$, regardless of the choice of Ansatz 1 or 2. On the other hand, there was a slight difference in $\Phi_\parallel(\boldsymbol{\chi}, t)$ between Ansatzes 1 and 2. These different changes contribute to the changes in the one-dimensional spectra at low wavenumbers. As discussed later, the energy changes at $\pi/2$ in $\Phi_\perp(\boldsymbol{\chi}, t)$ yield large changes at low wavenumbers in the compressed direction, whereas there are no changes in the longitudinal one-dimensional spectra at low wavenumbers because the energy remains at $\pi/2$ in $\Phi_\parallel(\boldsymbol{\chi}, t)$.

As shown in figures 2 and 3, the changes in the energy spectral tensors strongly depend on the initial distributions of the energy spectral tensors. Thus, we can interpret the change in the angular distribution as the effect of the initial anisotropy. When the initial anisotropy is strong, as discussed later, the amplifications of velocity variances are larger than in the case of homogeneous isotropic turbulence. These results suggest that the change in turbulence after compression is different for the near and far regions of the grid turbulence. In fact, these differences have been reported by Agui *et al.* (2005). Regardless of the initial energy spectral tensors, the distribution of $\Phi_\parallel(\boldsymbol{\chi}, t)$ tends to concentrate at $\theta = \pi/2$, whereas that of $\Phi_\perp(\boldsymbol{\chi}, t)$ tends to concentrate at $\theta = \pi/4$.

https://doi.org/10.1017/jfm.2016.313 Published online by Cambridge University Press

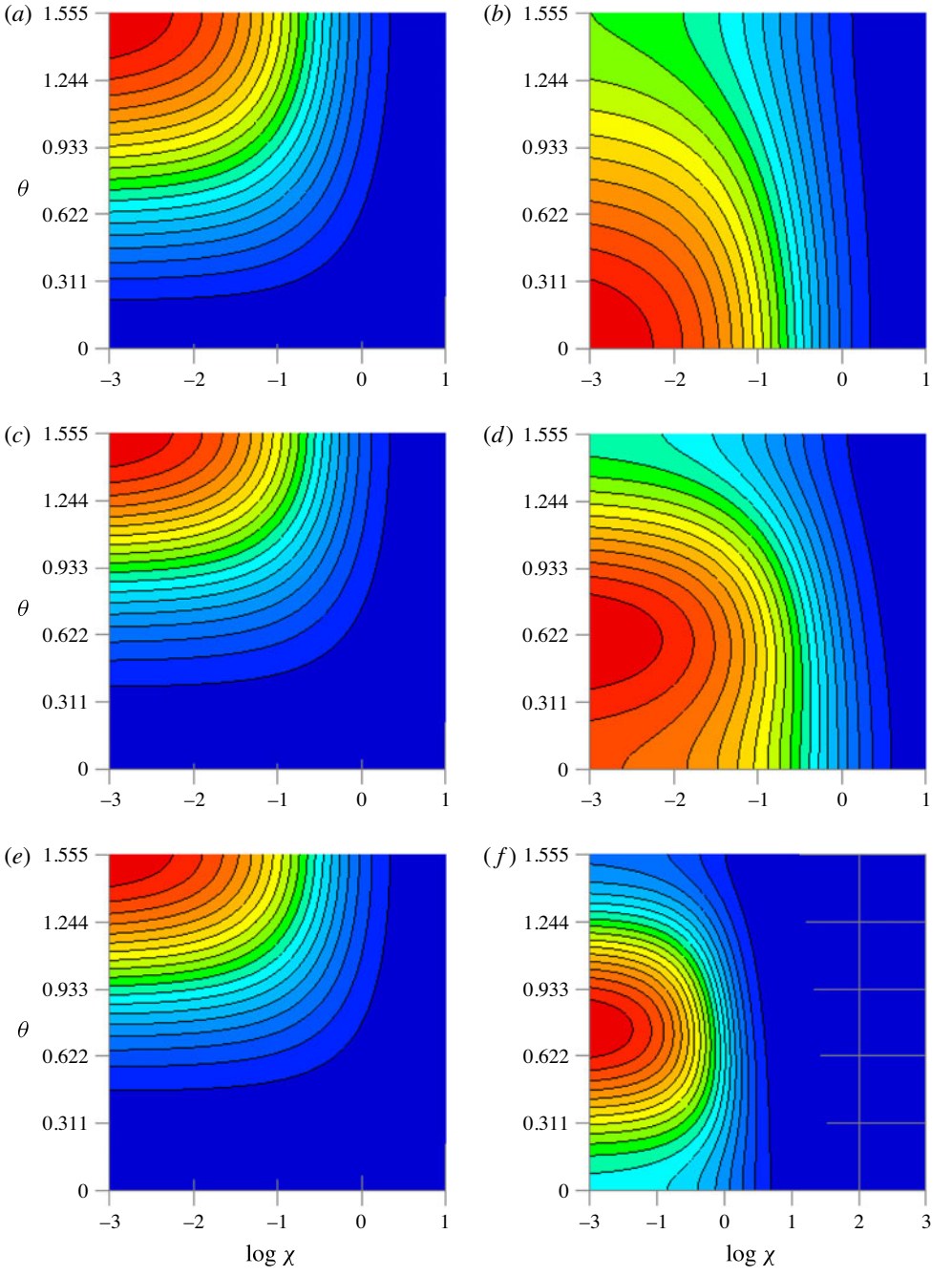


FIGURE 2. (Colour online) The angular distribution of the energy spectral tensors in homogeneous isotropic turbulence for model spectrum A (the Saffman–Pao model spectrum, $Re_\lambda = 10^2$) as an initial condition ($\log\chi$–θ plot). (*a*,*c*,*e*) The angular distribution of $\Phi_\parallel(\boldsymbol{\chi}, t)$. (*b*,*d*,*f*) The angular distribution of $\Phi_\perp(\boldsymbol{\chi}, t)$. Panels (*a*,*b*), (*c*,*d*) and (*e*,*f*) correspond to $\overline{\rho}/\rho_0 = 1$, $\overline{\rho}/\rho_0 = 2$ and $\overline{\rho}/\rho_0 = 4$ respectively. It should be noted that each colour contour is normalized by the maximum value in each figure.

https://doi.org/10.1017/jfm.2016.313 Published online by Cambridge University Press

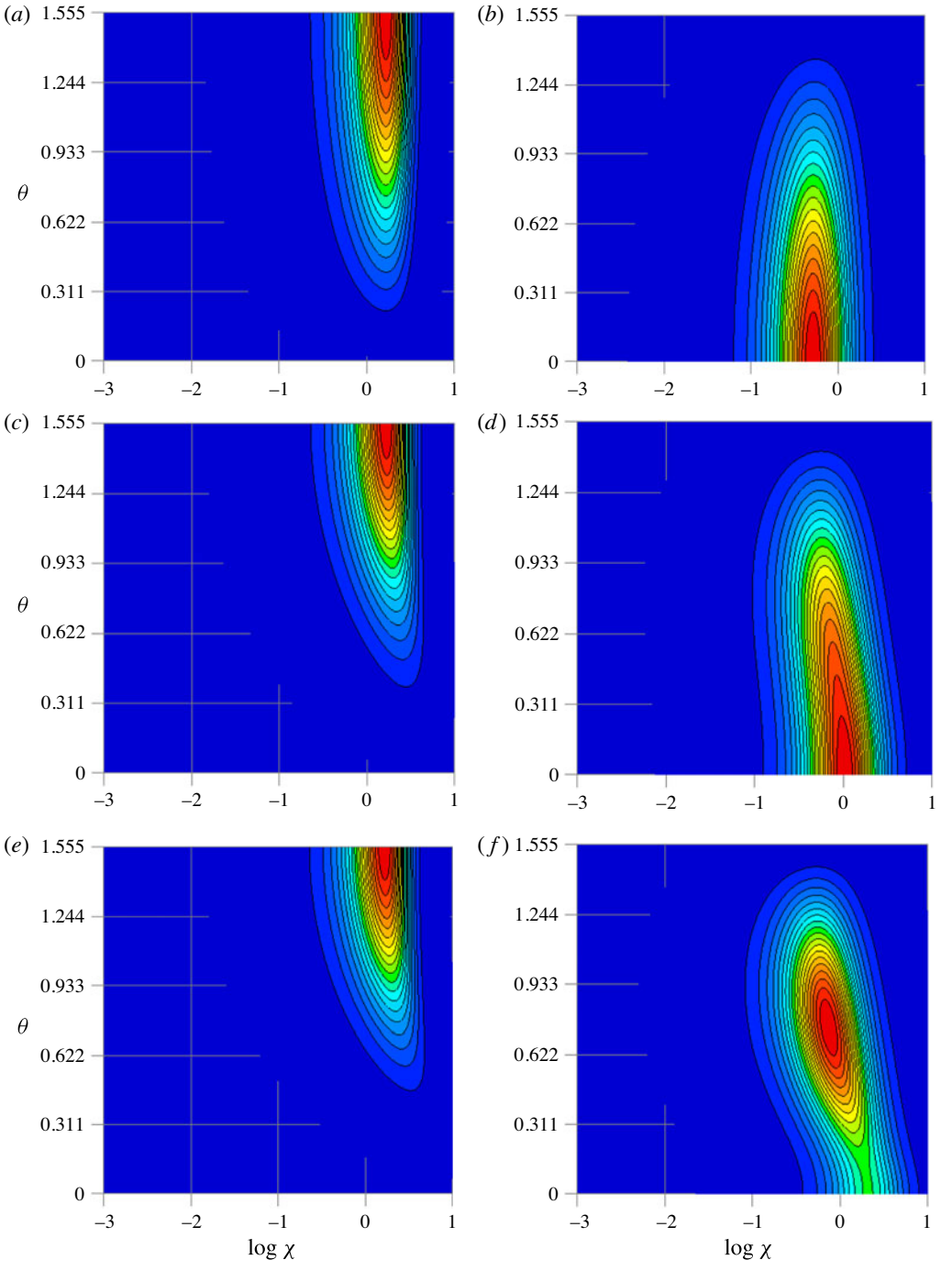


FIGURE 3. (Colour online) The same data as figure 2 but for model spectrum B with exponential form and $R_u = 7/4$.

https://doi.org/10.1017/jfm.2016.313 Published online by Cambridge University Press

5.2. *Velocity variances*

When isotropic initial conditions are considered, $Q^{(1)}(k) = Q^{(2)}(k) = E(k)/4\pi k^2$. From (3.6), (3.9) and (3.10), the energy spectral tensors are given by

$$\Phi_{\parallel}(\boldsymbol{\chi}, t) = \frac{E(k)}{4\pi k^2}[P^2 \sin^2\theta + Q^2 \cos^2\theta + 2PQ \sin 2\theta], \tag{5.1}$$

$$\Phi_{\perp}(\boldsymbol{\chi}, t) = \frac{E(k)}{8\pi k^2}[1 + P^2 \cos^2\theta + Q^2 \sin^2\theta - 2PQ \sin 2\theta], \tag{5.2}$$

$$\Phi_{ll}(\boldsymbol{\chi}, t) = \frac{E(k)}{4\pi k^2}[1 + P^2 + Q^2], \tag{5.3}$$

where

$$K^s(0) = \int_0^\infty \mathrm{d}k\, E(k) \tag{5.4}$$

is the initial TKE of the solenoidal mode. The variances of the parallel and perpendicular velocity fluctuations are given by

$$\begin{aligned}\langle u_{\parallel}^2(t)\rangle &= \int \mathrm{d}\boldsymbol{\chi}\, \Phi_{\parallel}(\boldsymbol{\chi}, t) = \frac{1}{1+S_1 t}\int \mathrm{d}\boldsymbol{k}\, \Phi_{\parallel}(\boldsymbol{\chi}, t) \\ &= \frac{K^s(0)}{2}\frac{C^3}{C^2-1}\left[1 + (C^2-2)\frac{\tan^{-1}\sqrt{C^2-1}}{\sqrt{C^2-1}}\right], \end{aligned} \tag{5.5}$$

$$\begin{aligned}\langle u_{\perp}^2(t)\rangle &= \int \mathrm{d}\boldsymbol{\chi}\, \Phi_{\perp}(\boldsymbol{\chi}, t) \\ &= \frac{CK^s(0)}{2}\left[1 + \frac{C^2}{2(C^2-1)}\left(-1 + C^2\frac{\tan^{-1}\sqrt{C^2-1}}{\sqrt{C^2-1}}\right)\right], \end{aligned} \tag{5.6}$$

and the TKE of the solenoidal mode is given by

$$\begin{aligned}K^s(t) &= \frac{1}{2}\int \mathrm{d}\boldsymbol{\chi}\, \Phi_{ll}(\boldsymbol{\chi}, t) = \frac{1}{1+S_1 t}\int \mathrm{d}\boldsymbol{k}\, \Phi_{ll}(\boldsymbol{\chi}, t) \\ &= \frac{K^s(0)}{2}\left[C + C^3\frac{\tan^{-1}\sqrt{C^2-1}}{\sqrt{C^2-1}}\right], \end{aligned} \tag{5.7}$$

where $C = \overline{\rho}/\rho_0$. The limiting cases for (5.5) and (5.6) have been derived by Ribner & Tucker (1953). For Ansatzes 1 and 2, the changes in each velocity variance and TKE value are described in § C.1. As confirmed by Larsson & Lele (2009) using DNS, the maximum wavenumber, which corresponds to the resolution in the physical space, is important in turbulence–shock-wave interactions. Using RDT analysis, Jacquin *et al.* (1993) obtained the TKE after the compression using the integration range $[k_{0,min} : k_{0,max}]$ for the initial homogeneous isotropic turbulence. However, as shown in the experiment of Barre *et al.* (1996), the TKE at high wavenumbers increases behind a shock wave. Furthermore, Larsson & Lele (2009) showed that different numerical resolutions yielded different amplification ratios of velocity variance, and that their DNS results were different from those of Lee *et al.* (1997) and the LIA. Therefore, the maximum wavenumber, which corresponds to the resolution in the physical space, plays an important role in the statistical quantities of turbulence. In homogeneous

https://doi.org/10.1017/jfm.2016.313 Published online by Cambridge University Press

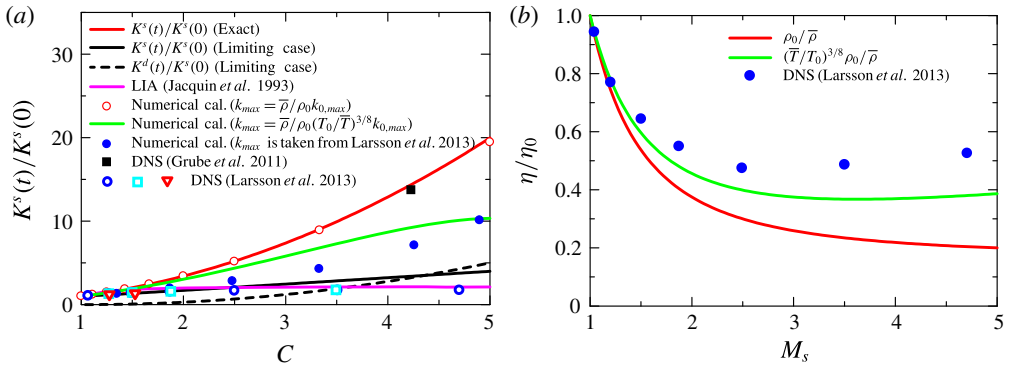


FIGURE 4. (Colour online) The amplification of the TKE versus the inviscid RDT solution for the initial homogeneous isotropic turbulence. Also included are the changes in the TKE from the LIA (near-field) result of Jacquin *et al.* (1993) and the DNS result of Grube *et al.* (2011) with the initial conditions $Re_\lambda = 26$, $M_t = 0.52$ and $M_1 = 3.46$, and Larsson *et al.* (2013) with the initial condition $Re_\lambda \approx 40$, where M_1 is the Mach number of the upstream of a shock wave.

turbulence, the TKE dissipation of the solenoidal mode is expressed by $\epsilon^s = \nu\langle\boldsymbol{\omega}^2\rangle$. Thus, the Kolmogorov length scale is expressed by $\eta = (\nu^2/\langle\boldsymbol{\omega}^2\rangle)^{1/4} = (\overline{\mu}^2/\overline{\rho}^2\langle\boldsymbol{\omega}^2\rangle)^{1/4}$, and the ratio between the Kolmogorov length scales after and before the interaction with a shock wave can be written as follows using $\sqrt{\langle\boldsymbol{\omega}^2\rangle}/\sqrt{\langle\boldsymbol{\omega}_0^2\rangle} \sim \overline{\rho}/\rho_0$ (Mahesh *et al.* 1997):

$$\frac{k_{0,max}}{k_{max}} = \frac{\eta}{\eta_0} = \left(\frac{\overline{\mu}^2\rho_0^4}{\mu_0^2\overline{\rho}^4}\right)^{1/4} = \left(\frac{\rho_0^4}{\overline{\rho}^4}f(\overline{T})\right)^{1/4}, \tag{5.8}$$

where $(\overline{\mu}/\mu_0)^2 = f(\overline{T})$ indicates that $\overline{\mu}$ is an increasing function of temperature $\overline{T}$. Larsson & Lele (2009) proposed a maximum wavenumber of $k_{max}/k_{0,max} = (\overline{\rho}/\rho_0)(T_0/\overline{T})^{3/8}$. Here, we adopted a maximum wavenumber of $k_{max} > (\overline{\rho}/\rho_0)k_{0,max}$ in the numerical calculation. Figure 4(*a*,*b*) shows the changes in the TKE and the changes in $\eta/\eta_0 (= k_{0,max}/k_{max})$. When we set the maximum wavenumber to $k_{max} > (\overline{\rho}/\rho_0)k_{0,max}$, the obtained results agreed with the exact solution (5.7). On the other hand, when we set the maximum wavenumber to $k_{max}/k_{0,max} = (\overline{\rho}/\rho_0)(T_0/\overline{T})^{3/8}$ as used in Larsson & Lele (2009) and Larsson *et al.* (2013), the TKE amplification was underestimated in the RDT analysis. As confirmed by the high-resolution DNS of Larsson & Lele (2009), the obtained results depend on the resolution. Furthermore, our RDT results suggest that the dependence on the resolution for the statistical quantities becomes remarkable with increase of Mach number. Thus, RDT analysis strongly suggests that high-resolution DNS is needed to obtain accurate results for turbulence–shock-wave interactions, especially for high-Mach-number flows. Of course, RDT is based on a linear theory, and the requirements of grid resolution for high-Mach-number flows should be carefully examined using DNS in future studies. The TKE amplification of the DNS results of Grube *et al.* (2011) is shown in figure 4; their results are in good agreement with the RDT analysis. The LIA result in the near field (Jacquin *et al.* 1993) is also included in figure 4. Based on this result, $k_{max} > (\overline{\rho}/\rho_0)k_{0,max}$ is used for the RDT analysis with non-zero viscosity in § 6.

Figure 5(*a*) shows the amplification of the TKE for initial homogeneous axisymmetric turbulence. The amplification of the TKE depends on the initial degree of

https://doi.org/10.1017/jfm.2016.313 Published online by Cambridge University Press

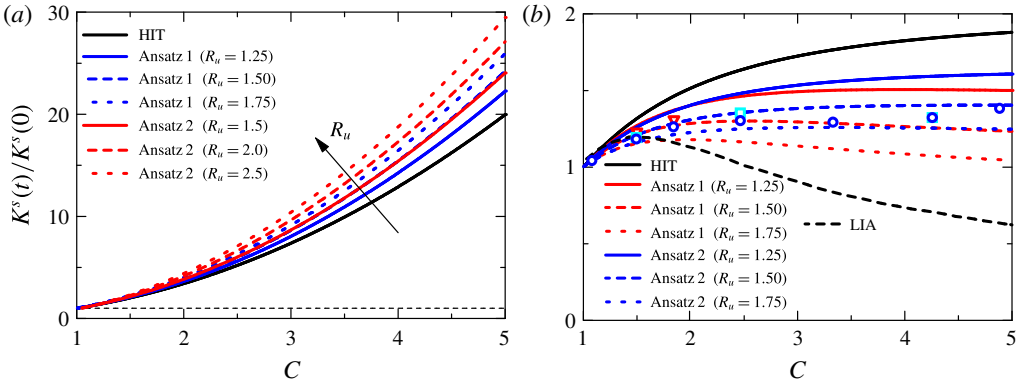


FIGURE 5. (Colour online) (*a*) The amplification of the TKE versus the inviscid RDT solution for initial homogeneous axisymmetric turbulence. (*b*) The changes in $\langle u_\parallel^2(t)\rangle/\langle u_\parallel^2(0)\rangle/(\langle u_\perp^2(t)\rangle/\langle u_\perp^2(0)\rangle)$. The symbols are taken from the DNS of Larsson *et al.* (2013); their results correspond to the post-shock turbulence anisotropy in the far field.

anisotropy; however, there is almost no dependence on the difference between Ansatzes 1 and 2. As discussed later, the amplification of $\langle u_\perp^2(t)\rangle$ contributes to the amplification of the TKE for the initial homogeneous axisymmetric turbulence. Figure 5(*b*) shows the changes in velocity anisotropy $\langle u_\parallel^2(t)\rangle/\langle u_\parallel^2(0)\rangle/(\langle u_\perp^2(t)\rangle/\langle u_\perp^2(0)\rangle)$. The results of Larsson *et al.* (2013) for the far region are also included for reference. The changes in anisotropy against $\overline{\rho}/\rho_0$ for RDT are closer to the DNS results rather than the LIA result. Here, it is worth mentioning the difference between RDT and the LIA. First, the changes in the TKE in the near regions are associated with the energy transfer from the acoustic potential energy in the LIA. However, such changes are not incorporated into RDT. Thus, the predictive capabilities of the RDT analysis for turbulence–shock interaction are limited to only the vicinity of the shock wave. In the vicinity of the shock wave, the RDT result qualitatively agrees with the DNS result (Larsson & Lele 2009) in that the parallel component of the velocity fluctuations is amplified more than the perpendicular component. However, the LIA result shows the opposite result for $M_s = 2.0$ (Lee *et al.* 1997). This means that RDT is more accurate in the vicinity of the shock wave, whereas it cannot predict the statistical quantities for the far field. Then, RDT does not take into account of the entropy fluctuations. It is known that the entropy fluctuations are more significant than the acoustic fluctuations for high-Mach-number flows. Thus, the present RDT analysis is no longer valid for an inflow having the entropy fluctuations.

Figure 6 shows the changes in $\langle u_\parallel^2(t)\rangle$ and $\langle u_\perp^2(t)\rangle$. As shown in figure 6, the changes in the variance of each velocity component depend on the initial degree of anisotropy. For the changes in $\langle u_\perp^2(t)\rangle$, Ansatzes 1 and 2 yield different amplifications. When isotropic initial conditions are considered, the anisotropy of the velocity components is significant, but the anisotropy of the velocity components is not significant when the initial anisotropy is strong. However, this strong anisotropy cannot be seen in fully developed grid turbulence, as already shown in figure 5(*b*). Thus, the anisotropy of the velocity components may be a general consequence of homogeneous isotropic turbulence–shock-wave interactions.

As shown in the DNS of Grube *et al.* (2011), there is a slight contribution from the nonlinear term in the energy budget; however, it should be noted that the compressible

https://doi.org/10.1017/jfm.2016.313 Published online by Cambridge University Press

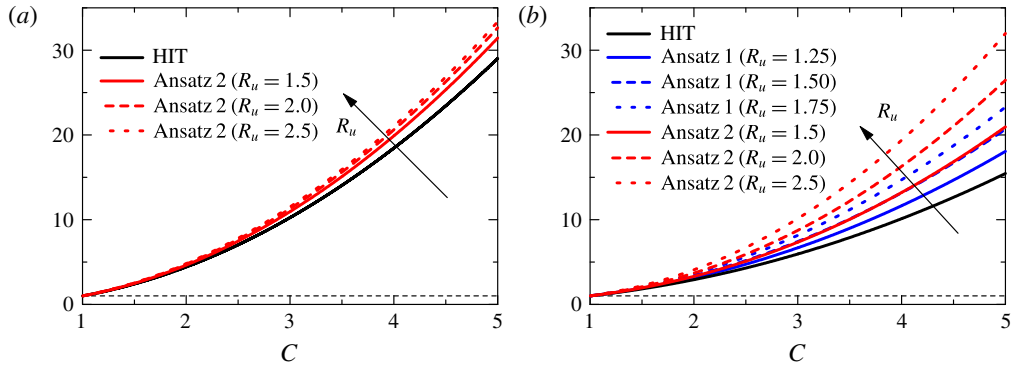


FIGURE 6. (Colour online) The amplification of velocity variances versus the inviscid RDT solution. (*a*) The variance of the parallel velocity components, $\langle u_\parallel^2(t)\rangle/\langle u_\parallel^2(0)\rangle$, and (*b*) the variance of the perpendicular velocity components, $\langle u_\perp^2(t)\rangle/\langle u_\perp^2(0)\rangle$. It should be noted that the changes in variance of the parallel velocity components for Ansatz 1 are the same as those for initial homogeneous isotropic turbulence, regardless of the initial anisotropy.

contribution is much larger than the nonlinear effect. In addition, there is a slight contribution from the baroclinic effect. Following Kevlahan & Hunt (1997), we simply evaluate the evolution of the nonlinear term of the solenoidal mode by means of the primitive perturbation method. By non-dimensionalizing the equations for $\hat{u}_i^s(\boldsymbol{\chi}, t)$ and $\boldsymbol{\chi}$ by the initial integral scale and the initial r.m.s. velocity u_0, (2.19) and (2.20) become

$$\frac{\mathrm{d}\hat{u}_i^s(\boldsymbol{\chi}, t)}{\mathrm{d}t} = -\frac{\chi^2}{Re_L\left(1-\dfrac{t}{\delta}\right)^{n(\kappa-1)-1}}\hat{u}_i^s(\boldsymbol{\chi}, t) + [\Pi_{i1}(\boldsymbol{\chi}) - P_{i1}(\boldsymbol{\chi})]\frac{-1}{\delta\left(1-\dfrac{t}{\delta}\right)}\hat{u}_1^s(\boldsymbol{\chi}, t) + N_i^s(\hat{\boldsymbol{u}}(\boldsymbol{\chi}, t), \boldsymbol{\chi}, t), \tag{5.9}$$

$$\chi_1(t) = \frac{k_1}{1-\dfrac{t}{\delta}}, \quad \chi_2(t) = k_2, \quad \chi_3(t) = k_3, \tag{5.10a–c}$$

where $\delta = (u_0/L)/|S_1| \ll 1$ is the ratio of the strain rate of the energy-containing eddies to the strength of compression and $Re_L = u_0 L/\nu$ is the Reynolds number; $N_i^s(\hat{\boldsymbol{u}}(\boldsymbol{\chi}, t), \boldsymbol{\chi}, t)$ is the nonlinear term. Furthermore, we change the variable $\tau = t/\delta$ in the dimensionless equations, and the RDT equations become

$$\frac{\mathrm{d}\hat{u}_i^s(\boldsymbol{\chi}, \tau)}{\mathrm{d}\tau} = -\frac{\delta\chi^2}{Re_L(1-\tau)^{n(\kappa-1)-1}}\hat{u}_i^s(\boldsymbol{\chi}, \tau) + [\Pi_{i1}(\boldsymbol{\chi}) - P_{i1}(\boldsymbol{\chi})]\frac{-1}{(1-\tau)}\hat{u}_1^s(\boldsymbol{\chi}, \tau) + \delta P_{ij}(\boldsymbol{\chi})N_j(\hat{\boldsymbol{u}}(\boldsymbol{\chi}, t), \boldsymbol{\chi}, \tau), \tag{5.11}$$

$$\chi_1(\tau) = \frac{k_1}{1-\tau}, \quad \chi_2(\tau) = k_2, \quad \chi_3(\tau) = k_3. \tag{5.12a–c}$$

By expanding $\hat{u}_i(\boldsymbol{\chi}, t)$ as a perturbation series in the ordering parameter δ, we obtain

$$\hat{u}_i(\boldsymbol{\chi}, t) = \hat{u}_i^{(0)}(\boldsymbol{\chi}, t) + \delta\hat{u}_i^{(1)}(\boldsymbol{\chi}, t) + O(\delta^2). \tag{5.13}$$

https://doi.org/10.1017/jfm.2016.313 Published online by Cambridge University Press

On equating the powers of δ, the zeroth-order equation implies neglecting the nonlinear terms, which are of order δ (while retaining the viscous terms), which leads to the following solutions:

$$\hat{u}_1^{s(0)}(\boldsymbol{\chi}, \tau) = \beta_1(\boldsymbol{k}, \tau)\hat{u}_1^s(\boldsymbol{k}, 0)f_v(\boldsymbol{k}, \tau), \tag{5.14}$$

$$\hat{u}_2^{s(0)}(\boldsymbol{\chi}, \tau) = \beta_2(\boldsymbol{k}, \tau)\hat{u}_1^s(\boldsymbol{k}, 0)f_v(\boldsymbol{k}, \tau) + \hat{u}_2^s(\boldsymbol{k}, 0)f_v(\boldsymbol{k}, \tau), \tag{5.15}$$

$$\hat{u}_3^{s(0)}(\boldsymbol{\chi}, \tau) = \beta_3(\boldsymbol{k}, \tau)\hat{u}_1^s(\boldsymbol{k}, 0)f_v(\boldsymbol{k}, \tau) + \hat{u}_3^s(\boldsymbol{k}, 0)f_v(\boldsymbol{k}, \tau), \tag{5.16}$$

where the $\beta_i(\boldsymbol{k}, \tau)$ are given by

$$\beta_1(\boldsymbol{k}, \tau) = \frac{k^2(1-\tau)}{k_1^2 + k_{23}^2(1-\tau)^2}, \tag{5.17}$$

$$\beta_i(\boldsymbol{k}, \tau) = -\frac{k_1 k_i \tau(2-\tau)}{k_1^2 + k_{23}^2(1-\tau)^2} \quad (i = 2 \text{ or } 3), \tag{5.18}$$

and $f_v(\boldsymbol{k}, \tau)$ is the viscous decay factor, which is given by

$$f_v(\boldsymbol{k}, \tau) = \exp\left[\frac{1}{Re_L}\left[\frac{k_1^2((1-\tau)^{n(1-\kappa)} - 1)}{n(1-\kappa)} + \frac{k_{23}^2((1-\tau)^{n(1-\kappa)+2} - 1)}{n(1-\kappa)+2}\right]\right]. \tag{5.19}$$

The nonlinear terms of the solenoidal mode are expanded in terms of $\hat{\boldsymbol{u}}^{(0)}(\boldsymbol{\chi}, t)$ as

$$\begin{aligned} N_i^s(\boldsymbol{\chi}, \tau) &= -\imath P_{ij}(\boldsymbol{\chi}) \int_{\boldsymbol{\chi}=\boldsymbol{p}+\boldsymbol{q}} \mathrm{d}\boldsymbol{p}\, q_n \hat{u}_n(\boldsymbol{p}, \tau)\hat{u}_j(\boldsymbol{q}, \tau) \\ &= P_{ij}(\boldsymbol{\chi})N_j^{(0)}(\hat{\boldsymbol{u}}^{(0)}(\boldsymbol{\chi}, \tau), \boldsymbol{\chi}, \tau) + O(\delta), \end{aligned} \tag{5.20}$$

where $\boldsymbol{\chi} = \boldsymbol{p} + \boldsymbol{q}$ is called a resonant triad condition, which is the hallmark of incompressible fluids, whereas $\boldsymbol{\chi} = \boldsymbol{p} + \boldsymbol{q} + \boldsymbol{r}$ appears in compressible fluids without the assumption of $\overline{\rho} \gg \rho'$. Here, the zeroth- and first-order nonlinear terms are shown in figure 7 using the diagram representation. In the diagram representation of the perturbation series, the nonlinear terms can be written by representing the main constituents such as $\hat{\boldsymbol{u}}^{(0)}$, $G^{(0)}$ and the projectors (2.15). As shown in figure 7, there are four convolutions in the zeroth-order nonlinear term. The first-order correction, $\hat{u}_i^{s(1)}(\boldsymbol{\chi}, \tau)$, to the RDT approximation is the solution to the equation

$$\begin{aligned} \frac{\mathrm{d}\hat{u}_i^{s(1)}(\boldsymbol{\chi}, \tau)}{\mathrm{d}\tau} &= -\frac{\delta\chi^2}{Re_L(1-\tau)^{n(\kappa-1)-1}}\hat{u}_i^{s(1)}(\boldsymbol{\chi}, \tau) + [\Pi_{i1}(\boldsymbol{\chi}) - P_{i1}(\boldsymbol{\chi})]\frac{-1}{(1-\tau)}\hat{u}_1^{s(1)}(\boldsymbol{\chi}, \tau) \\ &\quad + P_{ij}(\boldsymbol{\chi})N_j^{(0)}(\hat{\boldsymbol{u}}(\boldsymbol{\chi}, t), \boldsymbol{\chi}, \tau), \end{aligned} \tag{5.21}$$

where

$$\hat{u}_i^{s(1)}(\boldsymbol{\chi}, \tau) = \int_0^\tau \mathrm{d}s\, G_{im}^{s(0)}(\boldsymbol{\chi}, \tau, s)P_{mj}(\boldsymbol{\chi})N_j^{(0)}(\hat{\boldsymbol{u}}^{(0)}(\boldsymbol{\chi}, s), \boldsymbol{\chi}, s). \tag{5.22}$$

Here,

$$G_{1m}^{s(0)}(\boldsymbol{\chi}, \tau, s) = \beta_1(\boldsymbol{k}, \tau)\beta_1^{-1}(\boldsymbol{k}, s)f_v(\boldsymbol{k}, \tau)f_v^{-1}(\boldsymbol{k}, s)P_{1m}(\boldsymbol{\chi}), \tag{5.23}$$

$$\begin{aligned} G_{im}^{s(0)}(\boldsymbol{\chi}, \tau, s) &= (\beta_i(\boldsymbol{k}, \tau) - \beta_i(\boldsymbol{k}, s))\beta_1^{-1}(\boldsymbol{k}, s)f_v(\boldsymbol{k}, \tau)f_v^{-1}(\boldsymbol{k}, s)P_{1m}(\boldsymbol{\chi}) \\ &\quad + f_v(\boldsymbol{k}, \tau)f_v^{-1}(\boldsymbol{k}, s)P_{im}(\boldsymbol{\chi}) \quad (i = 2 \text{ or } 3). \end{aligned} \tag{5.24}$$

https://doi.org/10.1017/jfm.2016.313 Published online by Cambridge University Press

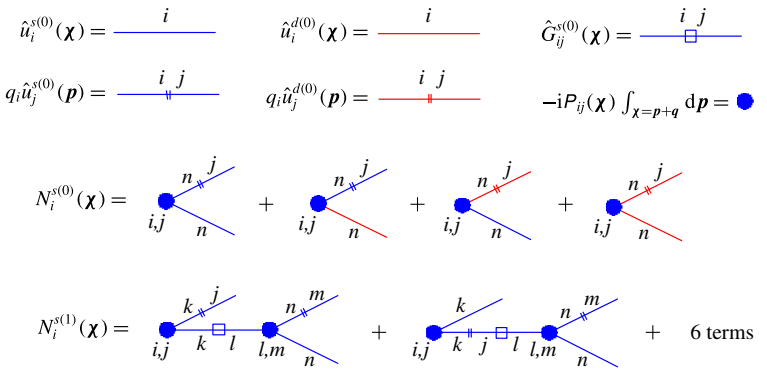


FIGURE 7. (Colour online) Diagram representation of the nonlinear terms. The blue lines correspond to the solenoidal mode; the red lines correspond to the dilatational mode; the $\hat{\boldsymbol{u}}^{s(0)}$ correspond to the RDT solutions (5.14)–(5.16).

In the zeroth nonlinear term, the largest contribution to the first-order correction $\hat{u}_i^{s(1)}(\boldsymbol{\chi}, \tau)$ to the RDT approximations is the convolution of the solenoidal modes when the initial conditions consist of the solenoidal mode. In fact, the contribution of the dilatational mode to the amplification of the TKE is less than that of the solenoidal mode (Jacquin *et al.* 1993). Thus, the evolutions of both the solenoidal mode and the dilatational mode are primarily caused by the change in the solenoidal mode (blue lines in figure 7), and the contribution of the first-order correction can be interpreted as an indirect effect of the Rankine–Hugoniot relation for any perturbation manner.

Regarding the answer to the first question of Andreopoulos *et al.* (2000), in this study, we cannot concretely determine how much of the TKE amplification after the interaction is caused solely by the Rankine–Hugoniot relation, because some causes of TKE amplification were neglected, e.g. the curved shock effect, the baroclinic effect, and so on. However, the present RDT analysis implies that the amplification of the TKE after the interaction is a direct consequence of the Rankine–Hugoniot relation, because the RDT governing equations for one-dimensional compression satisfy the Rankine–Hugoniot relation, and the effect of the nonlinear term contributes to the amplification of the TKE through the perturbation manner. Thus, the effect of the nonlinear term can be interpreted as an indirect consequence via the Rankine–Hugoniot relation.

5.3. *Vorticity variances*

When isotropic initial conditions are considered, the variances of the parallel and perpendicular vorticities after compression are given by

$$\langle\omega_\parallel^2(t)\rangle = \int \mathrm{d}\boldsymbol{\chi}\ \Omega_\parallel(\boldsymbol{\chi}, t) = C\langle\omega_\parallel^2(0)\rangle = \frac{C}{3}\langle\boldsymbol{\omega}^2(0)\rangle, \tag{5.25}$$

$$\langle\omega_\perp^2(t)\rangle = \int \mathrm{d}\boldsymbol{\chi}\ \Omega_\perp(\boldsymbol{\chi}, t) = \frac{C^3}{3}\langle\boldsymbol{\omega}^2(0)\rangle, \tag{5.26}$$

and the enstrophy is given by

$$\langle\boldsymbol{\omega}^2(t)\rangle = \int \mathrm{d}\boldsymbol{\chi}\ \chi^2\Phi_{ll}(\boldsymbol{\chi}, t) = \frac{C(2C^2+1)}{3}\langle\boldsymbol{\omega}^2(0)\rangle. \tag{5.27}$$

https://doi.org/10.1017/jfm.2016.313 Published online by Cambridge University Press

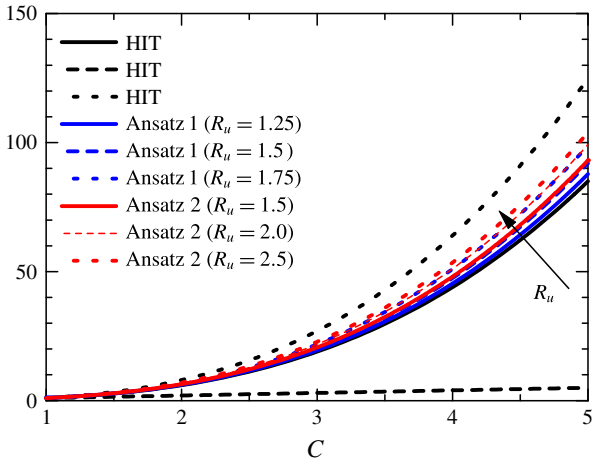


FIGURE 8. (Colour online) The amplification of the vorticity variances in inviscid RDT. The black solid, dashed and dotted lines correspond to the changes in $\langle \boldsymbol{\omega}^2(t)\rangle/\langle \boldsymbol{\omega}^2(0)\rangle$, $\langle \omega_\parallel^2(t)\rangle/\langle \omega_\parallel^2(0)\rangle$ and $\langle \omega_\perp^2(t)\rangle/\langle \omega_\perp^2(0)\rangle$ respectively, for initial homogeneous isotropic turbulence. The blue and red lines correspond to the changes in $\langle \boldsymbol{\omega}^2(t)\rangle/\langle \boldsymbol{\omega}^2(0)\rangle$ for the initial homogeneous axisymmetric turbulence of Ansatzes 1 and 2 respectively.

Regarding Ansatzes 1 and 2, the changes in each vorticity variance and enstrophy are described in § C.2. As shown in figure 8, the variance of the perpendicular vorticity, $\langle \omega_\perp^2\rangle$, is amplified more than that of the parallel vorticity, $\langle \omega_\parallel^2\rangle$. Similar results have been obtained in the DNS of Lee *et al.* (1993, 1997), Larsson & Lele (2009) and Grube *et al.* (2011). Regarding the limiting case of inviscid RDT analysis, $\langle \omega_\parallel^2\rangle$ does not change throughout the interaction. In the experiments of Agui *et al.* (2005), it was shown that $\langle \omega_\parallel^2\rangle$ was slightly reduced after the interaction. Using RDT analysis, their results may be interpreted as being caused by the lack of resolution (which may correspond to the limiting case in the RDT analysis). In fact, the high-resolution DNS of Grube *et al.* (2011) showed slight amplification of $\langle \omega_\parallel^2\rangle$.

Figure 9 shows the change in vorticity anisotropy. The results of Larsson & Lele (2009), Grube *et al.* (2011) and Larsson *et al.* (2013) are also shown. As discussed by Larsson & Lele (2009), the effect of resolution yields different results in the process of the return to isotropy behind a shock wave. In fact, the vorticity anisotropy of high-resolution DNS is closer to the RDT result than that of low-resolution DNS. Compared with the anisotropy of the velocity field, the anisotropy of the vorticity fields is significant. This phenomenon is due to the anisotropy at small scales after the interaction.

For the answer to the second question of Andreopoulos *et al.* (2000), the amplification of vorticity relates to the changes in wavenumber and the amplification of energy at high wavenumbers. Because the enstrophy can be calculated from (5.27), the integrand is given by $\chi^2\Phi_{ii}(\boldsymbol{\chi}, t)$, which can be approximated by $C^2k_1^2\Phi_{ii}(\boldsymbol{\chi}, t)$ by neglecting the related term k_{23}^2. Thus, the vorticity fluctuations are amplified more than the velocity fluctuations with order $C^2(=(\overline{\rho}/\rho_0)^2)$. Then, as described later, the shock-induced compression transfers energy to the fluctuating components, and redistributes energy in the Fourier space. As a consequence of these effects, the energy at small eddies is amplified and contributes to the amplification of vorticity fluctuations.

https://doi.org/10.1017/jfm.2016.313 Published online by Cambridge University Press

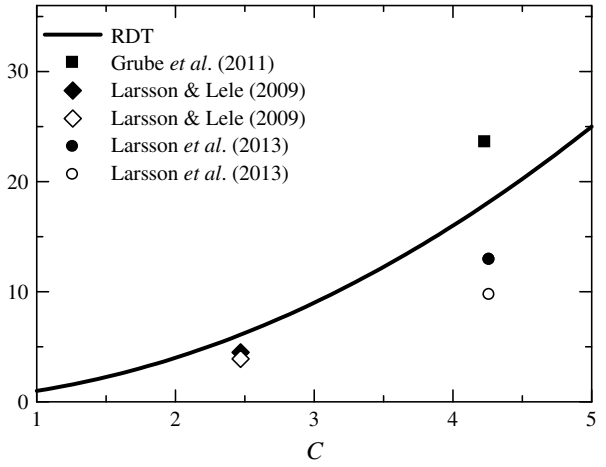


FIGURE 9. The change in vorticity anisotropy $\langle\omega_\perp^2\rangle/\langle\omega_\parallel^2\rangle$. We also present the DNS results of Larsson & Lele (2009), Grube *et al.* (2011) and Larsson *et al.* (2013). The black and white diamonds correspond to the DNS results of the initial conditions $M_s = 1.87$ and $M_t = 0.22$, and grids with 1040×384^2 and 174×64^2 respectively (Larsson & Lele 2009). The black and white circles correspond to the DNS results of the initial conditions $Re_\lambda = 40$ and $Re_\lambda = 74$ with $M_s = 3.5$ and $M_t = 0.16$ respectively (Larsson *et al.* 2013). The initial conditions of Grube *et al.* (2011) are the same as those in figure 4(*a*).

5.4. *Spectra*

The one-dimensional energy spectrum for the χ_1 direction is given by

$$\Theta_{ij}(\chi_1, t) = \int_0^\infty \int_0^\infty \Phi_{ij}(\boldsymbol{\chi}, t)\,\mathrm{d}\chi_2\,\mathrm{d}\chi_3 = \int_{\chi_1}^\infty \int_0^{2\pi} \Phi_{ij}(\boldsymbol{\chi}, t)\chi\,\mathrm{d}\chi\,\mathrm{d}\phi. \tag{5.28}$$

Although one-dimensional energy spectra can be calculated analytically, we investigated them numerically because of the cumbersome algebra. Figure 10 shows the one-dimensional energy spectra in exponential form for initial conditions with $R_u = 7/4$ for Ansatz 1. We confirmed that the main differences between the exponential form and the von Kármán form are apparent at high wavenumbers. Similar results are obtained for Ansatz 2, although differences between Ansatzes 1 and 2 are apparent at low wavenumbers.

Regardless of the initial forms of the energy spectra, the energy at high wavenumbers is amplified more than that at low wavenumbers. Regarding the changes in energy spectra at low wavenumbers, the changes in $\Theta_\perp(\chi_|, t)$ are larger than those in $\Theta_\parallel(\chi_|, t)$. These results correspond to the changes in the integral length scales, as described later.

Regarding the changes in the normalized one-dimensional energy spectrum $\Theta_\parallel(\chi_|, t)/\langle u_\parallel^2(t)\rangle$, the RDT results qualitatively agree with the experimental results of Barre *et al.* (1996) and Agui *et al.* (2005); however, it should be noted that these results are different from the experimental results of Honkan & Andreopoulos (1992), who showed that the energy of large eddies is amplified more than that of small eddies. In RDT analysis, although turbulence is treated as homogeneous turbulence, inhomogeneous effects will appear in large eddy structures after interaction with a shock wave. However, RDT analysis may yield good results for changes in small eddies, because local homogeneities can be assumed for high-Reynolds-number flows.

https://doi.org/10.1017/jfm.2016.313 Published online by Cambridge University Press

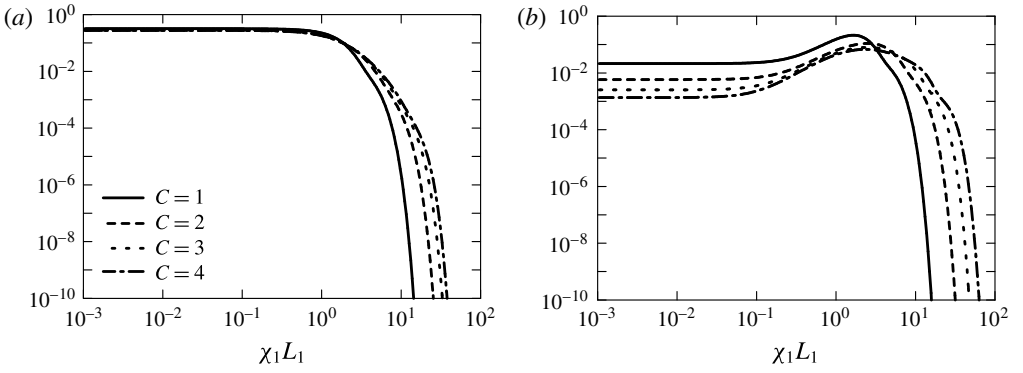


FIGURE 10. Normalized one-dimensional power spectra in the exponential form (*a*) $\Theta_{\parallel}(\chi_{\parallel}, t)/\langle u_{\parallel}^2(t)\rangle$ and (*b*) $\Theta_{\perp}(\chi_{\parallel}, t)/\langle u_{\perp}^2(t)\rangle$ for Ansatz 1 with $R_u = 7/4$ as an initial condition.

For the answer to the third question of Andreopoulos *et al.* (2000), the amplification of energy at high wavenumbers is due to the extension of wavenumber. In terms of energy exchange, the shock-induced compression transfers energy to the fluctuating components, and redistributes energy in the Fourier space. These energy transfers are seen at high wavenumbers; as a consequence, the distant triad interactions, $\max(k, p, q)/\min(k, p, q) \gg 1$, will be more dominant than the local triad interactions, $\max(k, p, q)/\min(k, p, q) \sim 1$, in the small eddies when nonlinear effects are considered. These conclusions are based on the basic principles of RDT analysis.

5.5. *Turbulence characteristic length scales*

The integral length scale $L_{ij,n}$ is defined by the integration of the cross-correlation coefficient $r_{ij}(\xi_n)$ from zero to infinity; it is given by

$$L_{ij,n}(t) = \int_0^\infty \mathrm{d}\xi\; r_{ij}(\xi_n) = \frac{1}{\langle u_i u_j\rangle} \int_0^\infty \mathrm{d}\xi\; \langle u_i(\boldsymbol{x}) u_j(\boldsymbol{x} + \xi_n)\rangle. \tag{5.29}$$

In homogeneous turbulence,

$$L_{ij,n}(t) = \frac{\pi}{\langle u_i u_j\rangle} \int_{-\infty}^{\infty} \mathrm{d}\boldsymbol{\chi}_m \int_{-\infty}^{\infty} \mathrm{d}\boldsymbol{\chi}_l\, \Phi_{ij}(\boldsymbol{\chi}, t)\,|_{\chi_n=0}, \tag{5.30}$$

where $\boldsymbol{\chi}_m (= \chi_m \boldsymbol{e}_m)$ is the vector orthogonal to $\boldsymbol{\chi}_n (= \chi_n \boldsymbol{e}_n)$ and $\boldsymbol{\chi}_l (= \chi_l \boldsymbol{e}_l)$ is the vector orthogonal to both $\boldsymbol{\chi}_m$ and $\boldsymbol{\chi}_n$. Therefore, the integral length scale can be calculated from the planar integral.

When isotropic initial conditions are considered, the longitudinal integral length scale (e.g. $L_{11,1} = L_{22,2} = L_{33,3}$) is defined as (Batchelor 1953)

$$L_f = \frac{3\pi}{4K^s} \int_0^\infty \frac{E(k)}{k}\, \mathrm{d}k, \tag{5.31}$$

where the lateral integral length scale is $L_g = 1/2 L_f$.

The analytical solutions of the integral length scales are presented in § C.3. Figure 11 shows the changes in the integral length scales for initial homogeneous

https://doi.org/10.1017/jfm.2016.313 Published online by Cambridge University Press

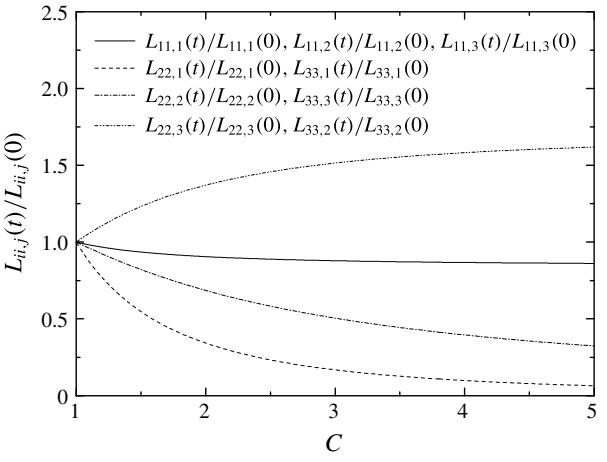


FIGURE 11. Changes in integral length scale in the inviscid RDT analysis.

isotropic turbulence. As shown in figure 11, most integral length scales (e.g. $L_{11,1}$, $L_{22,2}$ $(=L_{33,3})$, $L_{22,1}$ $(=L_{33,1})$ and $L_{11,2}$ $(=L_{11,3})$) decrease after the compression, whereas $L_{22,3}$ $(=L_{33,2})$ increases. In these integral length scales, $L_{22,1}$ $(=L_{33,1})$ is significantly reduced after the compression. When initial isotropic conditions are considered, there are no differences between $L_{11,1}$ and $L_{11,2}$ $(=L_{11,3})$; however, one can see the differences between them for initial homogeneous axisymmetric turbulence.

The Taylor microscale, $\lambda_{ii,j}$, is defined by

$$\lambda_{ii,j}(t) = \sqrt{\frac{\langle u_i^2 \rangle}{\left\langle \left(\dfrac{\partial u_i}{\partial x_j} \right)^2 \right\rangle}} = \sqrt{\frac{\displaystyle\int \mathrm{d}\boldsymbol{\chi}\ \Phi_{ii}(\boldsymbol{\chi}, t)}{\displaystyle\int \mathrm{d}\boldsymbol{\chi}\ \chi_j^2 \Phi_{ii}(\boldsymbol{\chi}, t)}} \quad \text{(no summation with respect to } i\text{)}. \tag{5.32}$$

When isotropic initial conditions are considered, the square of the longitudinal Taylor microscale λ_f^2 is given by

$$\lambda_f^2 = 5\frac{\langle \boldsymbol{u}^2 \rangle}{\langle \boldsymbol{\omega}^2 \rangle}, \tag{5.33}$$

and the square of the lateral Taylor microscale is $\lambda_g^2 = \lambda_f^2/2$. The analytical solutions of the Taylor microscales are described in § C.4. Figure 12 shows the changes in Taylor microscales for initial homogeneous isotropic turbulence. As shown in figure 12, most Taylor microscales (e.g. $\lambda_{11,1}$, $\lambda_{22,2}$ $(=\lambda_{33,3})$, $\lambda_{22,1}$ $(=\lambda_{33,1})$ and $\lambda_{11,2}$ $(=\lambda_{11,3})$) decrease after the compression, whereas $\lambda_{22,3}$ $(=\lambda_{33,2})$ increases. Unlike the changes in the integral length scales, there is a difference between the changes in $\lambda_{\parallel,|}$ and $\lambda_{\perp\perp,|}$. Regarding the length scales related to the parallel velocity components and the parallel direction, the reduction of Taylor microscales is larger than that of the integral length scales. On the other hand, regarding the length scales related to the perpendicular components, the changes in the integral length scales are larger than those of the Taylor microscales.

https://doi.org/10.1017/jfm.2016.313 Published online by Cambridge University Press

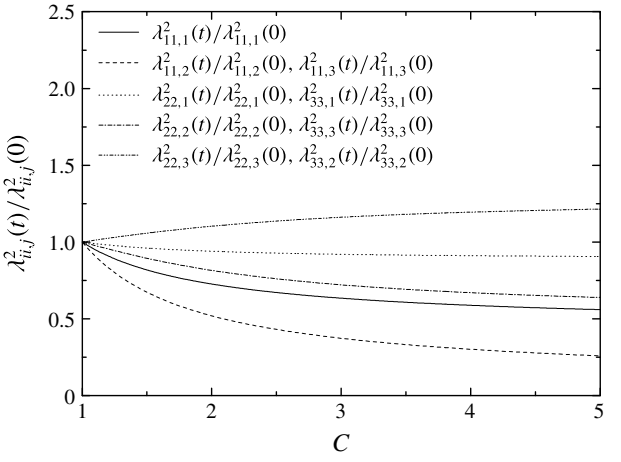


FIGURE 12. Changes in Taylor microscale in the inviscid RDT analysis.

To the best of our knowledge, the issue of whether $L_{22,3}$ $(=L_{33,2})$ and $\lambda_{22,3}$ $(=\lambda_{33,2})$ are reduced or amplified has not been investigated in previous studies. In RDT analysis, these length scales are amplified after the compression. The other length scales are reduced after the compression. These results qualitatively agree with those of previous experiments (e.g. Agui *et al.* 2005) and DNS (e.g. Lee *et al.* 1993; Hannappel & Friedrich 1995; Grube *et al.* 2011). The abovementioned results are part of the answer to the fourth question of Andreopoulos *et al.* (2000) related to the changes in the turbulent length scales. The changes in the dissipation length will be discussed later.

6. Results and discussion for RDT analysis with non-zero viscosity

We investigated the changes in TKE dissipation and dissipation length scale using model spectra A ($Re_\lambda = 10^2$ and 10^4).

The non-zero viscous solutions take the form (Hanazaki & Hunt 2004)

$$\hat{u}_i^s(\boldsymbol{\chi}, t) = D(t)\hat{u}_i^{s\,inv}(\boldsymbol{\chi}, t), \tag{6.1}$$

where the superscript '*inv*' denotes the inviscid solutions (2.31)–(2.33). Here, $D(t)$ is a function that satisfies

$$\left(\frac{\mathrm{d}}{\mathrm{d}t} + \nu(t)\chi^2\right) D(t) = 0. \tag{6.2}$$

With an initial condition $D(0) = 1$,

$$D(t) = \exp\left(-\int_0^t \mathrm{d}s\, \nu(s)\chi^2(s)\right) = \exp\left[-\frac{\nu_0}{S_1}\left[\frac{k_1^2}{n(1-\kappa)}((1+S_1t)^{n(1-\kappa)} - 1) + \frac{k_{23}^2}{n(1-\kappa)+2}((1+S_1t)^{n(1-\kappa)+2} - 1)\right]\right]. \tag{6.3}$$

https://doi.org/10.1017/jfm.2016.313 Published online by Cambridge University Press

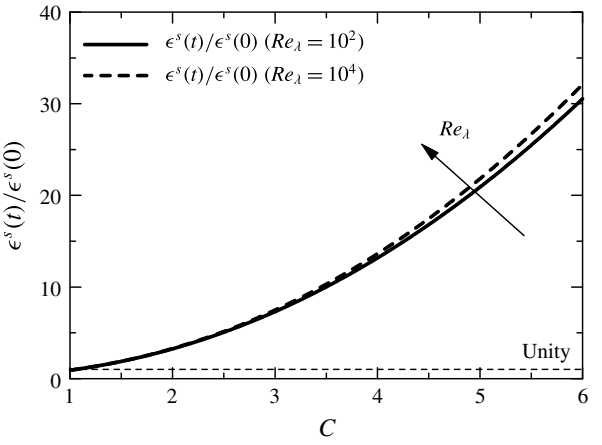


FIGURE 13. The amplification of the TKE dissipation rate of the solenoidal mode.

Rapid shock-induced compression does not break the symmetry of the statistical quantities of turbulence, as shown in RDT analysis and confirmed by DNS (Lee *et al.* 1993, 1997). The energy spectral tensors with non-zero viscosity after the compression are expressed by

$$\Phi_{\parallel}(\boldsymbol{\chi}, t) = D^2(t)\Phi_{\parallel}^{inv}(\boldsymbol{\chi}, t), \tag{6.4}$$

$$\Phi_{\perp}(\boldsymbol{\chi}, t) = D^2(t)\Phi_{\perp}^{inv}(\boldsymbol{\chi}, t). \tag{6.5}$$

6.1. *Turbulence kinetic energy dissipation rate*

The ensemble averaged TKE dissipation rate in a homogeneous compressible flow can be decomposed into the solenoidal mode, ϵ^s, and the dilatational mode, ϵ^d (Bertoglio, Bataille & Marion 2001),

$$\epsilon^s = \nu\langle\boldsymbol{\omega}^2\rangle, \tag{6.6}$$

$$\epsilon^d = \frac{4}{3}\nu\left\langle\left(\frac{\partial u_i^d}{\partial x_i}\right)^2\right\rangle. \tag{6.7}$$

In weakly compressible homogeneous isotropic turbulence, Bertoglio *et al.* (2001) showed that ϵ^d is related to ϵ^s via $\epsilon^d = \alpha_1 M_t^2 \epsilon^s$, where $\alpha_1 \approx 0.5$. Thus, the evolution of the dilatational TKE dissipation rate is assumed to be weak for one-dimensional compression when the initial velocity fields consist only of the solenoidal mode.

Figure 13 shows the changes in the TKE dissipation rate of the solenoidal mode. After the compression, the TKE dissipation rate of the solenoidal mode is amplified and there is a slight Reynolds number dependence. These results qualitatively agree with the experiments of Agui *et al.* (2005).

For the answer to the fifth question of Andreopoulos *et al.* (2000), the TKE dissipation rate of the solenodal mode is amplified after the compression. The TKE dissipation rate of the dilatational mode is also amplified after the compression because it is related to the amplification of the velocity fluctuation of the dilatational mode.

https://doi.org/10.1017/jfm.2016.313 Published online by Cambridge University Press

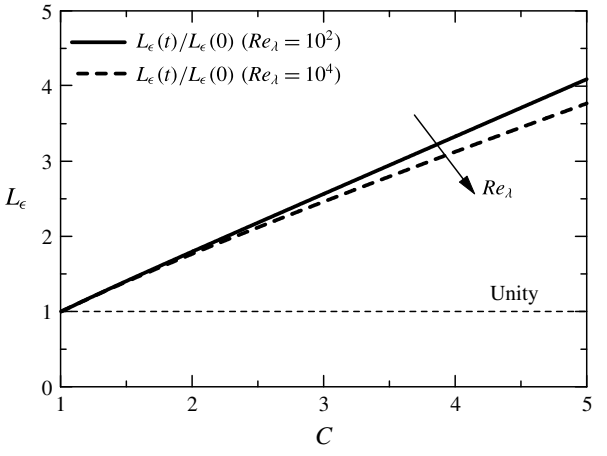


FIGURE 14. Changes in the dissipation scale.

6.2. *Dissipation length scale*

The dissipation length scale is defined by

$$L_\epsilon = \frac{K^{3/2}}{\epsilon}. \tag{6.8}$$

Figure 14 shows the changes in L_ϵ; it is amplified after the compression, and there is a slight Reynolds number dependence. The obtained results qualitatively agree with the experiments of Honkan & Andreopoulos (1992) and the DNS of Lee *et al.* (1997); however, Hannappel & Friedrich (1995) showed the opposite results. Because the dissipation length scale is a ratio of the amplification of the TKE and the amplification of the TKE dissipation rate, the changes in L_ϵ may be related to both the initial strength of the turbulent Mach number and the initial Reynolds number.

7. Conclusions

The interactions between turbulence and a shock wave were analytically investigated by means of RDT analysis for initial homogeneous isotropic and axisymmetric turbulence.

We attempted to answer the questions identified by Andreopoulos *et al.* (2000) within the linear theoretical framework. The main results are as follows.

(i) How much of the amplification of turbulence interacted with a shock wave is caused entirely by the Rankine–Hugoniot conditions?

Because the obtained results in RDT are based on the Rankine–Hugoniot relation, the effect of shock-induced compression can be interpreted as a direct consequence of the Rankine–Hugoniot relation. Nonlinear effects may have appeared as an indirect consequence of the Rankine–Hugoniot relation via the perturbation manner. The convolution of the solenoidal modes is dominant when the initial solenoidal velocity fields are given. Although RDT analysis does not consider the baroclinic effects and curved shock effects, these effects are considered to be smaller than those of the shock-induced compression and nonlinear effects. Thus, the amplifications of the TKE are caused primarily by the Rankine–Hugoniot relation.

https://doi.org/10.1017/jfm.2016.313 Published online by Cambridge University Press

(ii) Why are vorticity fluctuations amplified more than velocity fluctuations?

The amplification of vorticity relates to changes in wavenumber and the amplification of energy at high wavenumbers. Because the enstrophy can be calculated from the integral $(1/2)\langle\boldsymbol{\omega}^2(t)\rangle = (1/2)\int \mathrm{d}\boldsymbol{\chi}\ \Omega_{ii}(\boldsymbol{\chi}, t)$, the integrand is given by $\Omega_{ii}(\boldsymbol{\chi}, t) = \chi^2\Phi_{ii}(\boldsymbol{\chi}, t)$, which can be approximated by $C^2k_1^2\Phi_{ii}(\boldsymbol{\chi}, t)$ by neglecting the related term k_{23}^2. Thus, vorticity fluctuations are more amplified than velocity fluctuations with order $C^2(=(\overline{\rho}/\rho_0)^2)$.

(iii) Why is the energy of small eddies amplified more than that of large eddies?

The amplification of energy at high wavenumbers is due to the extension of wavenumber. Then, the forms of energy spectra may be important. The main difference is seen in the region of the exponential form at high wavenumbers (unlike the power law form).

(iv) Are the length scales of the incoming turbulence reduced or amplified through such interactions?

The integral length scales and the Taylor microscales are reduced for most cases. However, $L_{22,3}$ $(=L_{33,2})$ and $\lambda_{22,3}$ $(=\lambda_{33,2})$ are amplified. After the compression, the dissipation length scale is amplified and there is a slight Reynolds number dependence. Because the dissipation length scale is the ratio of the amplification of the TKE to the amplification of the TKE dissipation rate, the changes of dissipation length scale may be related to the initial strength of the turbulent Mach number and the initial Reynolds number.

(v) Is the TKE dissipation rate reduced?

The TKE dissipation rate of the solenoidal mode is amplified after compression, and there is a slight Reynolds number dependence. Although the kinematic viscosity is a decreasing function of $\overline{\rho}/\rho_0$, the increase in the enstrophy is larger than the decrease in the kinematic viscosity.

When the initial velocity fields are given by homogeneous axisymmetric turbulence, the amplification of the velocity and vorticity variances depends on both the initial degree of anisotropy and the angular distribution of the energy spectral tensor. The changes in parallel velocity variances depend on the energy distribution of the wave mode. Thus, different results are obtained between Ansatzes 1 and 2. Regardless of the initial energy spectra, the energies at high wavenumber are amplified more than those at low wavenumbers.

Acknowledgements

The authors would like to thank Dr C. Cambon (Ecole Centrale de Lyon) for his helpful comments. They also thank Mr K. Takeuchi (Nagoya University) and Mr K. Konishi (Nagoya University) for confirming the cumbersome analytical calculations. T.K. would like to thank the Leadership Development Program for Space Exploration and Research in the Nagoya University Program for Leading Graduate Schools for their financial support. This work was also supported by the Japanese Ministry of Education, Science and Culture through Grants-in-Aid (nos 22226014 and 25289030).

Appendix A

Here, we describe how to solve ODEs. This calculation method is valid for almost all RDT equations (e.g. stratified turbulence, rotational turbulence, pure shear strain and axisymmetric strain) and for the first step for closures such as direct interaction

https://doi.org/10.1017/jfm.2016.313 Published online by Cambridge University Press

approximation (DIA) families (e.g. weakly compressible homogeneous isotropic turbulence, stratified turbulence, low-Re_m magnetohydrodynamic (MHD) turbulence, and so on); however, this method is not valid for the dilatational mode RDT solution.

Using the eigenvalues, the transformation matrix $\boldsymbol{B}$ is given by

$$\boldsymbol{B}=\begin{bmatrix} 0 & \dfrac{k_{23}}{k_2}\imath & -\dfrac{k_{23}}{k_3}\imath \\ -\dfrac{k_3}{k_2} & 1 & \dfrac{k_2}{k_3} \\ 1 & \dfrac{k_3}{k_2} & 1 \end{bmatrix}, \tag{A 1}$$

and the determinant of $\boldsymbol{B}$ is given by

$$\mathrm{Det}\,\boldsymbol{B}=\frac{2k_{23}^3\imath}{k_2^2k_3}. \tag{A 2}$$

The inverse transformation matrix is given by

$$\boldsymbol{B}^{-1}=\frac{1}{k_{23}}\begin{bmatrix} 0 & -\dfrac{k_2k_3}{k_{23}} & \dfrac{k_2^2}{k_{23}} \\ -\dfrac{k_2}{2}\imath & \dfrac{k_2^2}{2k_{23}} & \dfrac{k_2k_3}{2k_{23}} \\ \dfrac{k_3}{2}\imath & \dfrac{k_2k_3}{2k_{23}} & \dfrac{k_3^2}{2k_{23}} \end{bmatrix}. \tag{A 3}$$

The diagonal matrix $\boldsymbol{D}$ consisting of the eigenvalues is given by

$$\boldsymbol{D}=\frac{S_1}{k_1^2+k_{23}^2(1+S_1t)^2}\begin{bmatrix} 0 & 0 & 0 \\ 0 & -k_{23}^2(1+S_1t)+\imath k_1k_{23} & 0 \\ 0 & 0 & -k_{23}^2(1+S_1t)-\imath k_1k_{23} \end{bmatrix}. \tag{A 4}$$

Because $\boldsymbol{B}^{-1}$ is not a function of t, after multiplying $\boldsymbol{B}^{-1}$ by (2.29) from the left side, one obtains

$$\frac{\mathrm{d}}{\mathrm{d}t}\underbrace{B_{\alpha i}^{-1}\hat{u}_i^s}_{y_\alpha}=B_{\alpha i}^{-1}A_{i\beta}\underbrace{B_{\beta\gamma}B_{\gamma j}^{-1}}_{\delta_{\beta j}}\hat{u}_j^s=D_{\alpha\gamma}\underbrace{B_{\gamma j}^{-1}\hat{u}_j^s}_{y_\gamma}. \tag{A 5}$$

For each component, we have

$$\frac{\mathrm{d}y_1(\boldsymbol{\chi},t)}{\mathrm{d}t}=0, \tag{A 6}$$

$$\frac{\mathrm{d}y_2(\boldsymbol{\chi},t)}{\mathrm{d}t}=\frac{S_1}{k_1^2+k_{23}^2(1+S_1t)^2}(-k_{23}^2(1+S_1t)+\imath k_1k_{23})y_2(\boldsymbol{\chi},t), \tag{A 7}$$

$$\frac{\mathrm{d}y_3(\boldsymbol{\chi},t)}{\mathrm{d}t}=\frac{S_1}{k_1^2+k_{23}^2(1+S_1t)^2}(-k_{23}^2(1+S_1t)-\imath k_1k_{23})y_3(\boldsymbol{\chi},t). \tag{A 8}$$

https://doi.org/10.1017/jfm.2016.313 Published online by Cambridge University Press

The solution of $\boldsymbol{y}$ can be obtained after some algebra using the separation of variables

$$\begin{bmatrix} y_1(\boldsymbol{\chi}, t) \\ y_2(\boldsymbol{\chi}, t) \\ y_3(\boldsymbol{\chi}, t) \end{bmatrix} = \begin{bmatrix} y_1(\boldsymbol{k}, 0) \\ y_2(\boldsymbol{k}, 0)\dfrac{k_1^2 + k_{23}^2(1+S_1t) + \imath k_1 k_{23} S_1 t}{k_1^2 + k_{23}^2(1+S_1t)^2} \\ y_3(\boldsymbol{k}, 0)\dfrac{k_1^2 + k_{23}^2(1+S_1t) + \imath k_1 k_{23} S_1 t}{k_1^2 + k_{23}^2(1+S_1t)^2} \end{bmatrix}. \tag{A 9}$$

Initial components $\boldsymbol{y}(\boldsymbol{k}, 0)$ can be obtained via $\boldsymbol{y}(\boldsymbol{k}, 0) = \boldsymbol{B}^{-1}\hat{\boldsymbol{u}}^s(\boldsymbol{k}, 0)$, which are given by

$$\begin{bmatrix} y_1(\boldsymbol{k}, 0) \\ y_2(\boldsymbol{k}, 0) \\ y_3(\boldsymbol{k}, 0) \end{bmatrix} = \begin{bmatrix} -\dfrac{k_2 k_3}{k_{23}^2}\hat{u}_2(\boldsymbol{k}, 0) + \dfrac{k_2^2}{k_{23}^2}\hat{u}_3(\boldsymbol{k}, 0) \\ -\dfrac{k_2 \imath}{2k_{23}}\hat{u}_1(\boldsymbol{k}, 0) + \dfrac{k_2^2}{2k_{23}^2}\hat{u}_2(\boldsymbol{k}, 0) + \dfrac{k_2 k_3}{2k_{23}^2}\hat{u}_3(\boldsymbol{k}, 0) \\ -\dfrac{k_3 \imath}{2k_{23}}\hat{u}_1(\boldsymbol{k}, 0) + \dfrac{k_2 k_3}{2k_{23}^2}\hat{u}_2(\boldsymbol{k}, 0) + \dfrac{k_3^2}{2k_{23}^2}\hat{u}_3(\boldsymbol{k}, 0) \end{bmatrix}. \tag{A 10}$$

From the relation $\hat{\boldsymbol{u}}^s(\boldsymbol{\chi}, t) = \boldsymbol{B}\boldsymbol{y}(\boldsymbol{\chi}, t)$, we obtain

$$\begin{aligned} \begin{bmatrix} \hat{u}_1^s(\boldsymbol{\chi}, t) \\ \hat{u}_2^s(\boldsymbol{\chi}, t) \\ \hat{u}_3^s(\boldsymbol{\chi}, t) \end{bmatrix} &= \begin{bmatrix} P\hat{u}_1^s(\boldsymbol{k}, 0) - \dfrac{k_2 Q}{k_{23}}\hat{u}_2^s(\boldsymbol{k}, 0) - \dfrac{k_3 Q}{k_{23}}\hat{u}_3^s(\boldsymbol{k}, 0) \\ \dfrac{k_2 Q}{k_{23}}\hat{u}_1^s(\boldsymbol{k}, 0) + \dfrac{k_3^2 + k_2^2 P}{k_{23}^2}\hat{u}_2^s(\boldsymbol{k}, 0) + \dfrac{k_2 k_3}{k_{23}^2}(P-1)\hat{u}_3^s(\boldsymbol{k}, 0) \\ \dfrac{k_3 Q}{k_{23}}\hat{u}_1^s(\boldsymbol{k}, 0) + \dfrac{k_2 k_3}{k_{23}^2}(P-1)\hat{u}_2^s(\boldsymbol{k}, 0) + \dfrac{k_2^2 + k_3^2 P}{k_{23}^2}\hat{u}_3^s(\boldsymbol{k}, 0) \end{bmatrix} \\ &= \begin{bmatrix} \dfrac{k^2(1+S_1t)}{k_1^2 + k_{23}^2(1+S_1t)^2}\hat{u}_1^s(\boldsymbol{k}, 0) \\ \dfrac{k_1 k_2 S_1 t(2+S_1t)}{k_1^2 + k_{23}^2(1+S_1t)^2}\hat{u}_1^s(\boldsymbol{k}, 0) + \hat{u}_2^s(\boldsymbol{k}, 0) \\ \dfrac{k_1 k_2 S_1 t(2+S_1t)}{k_1^2 + k_{23}^2(1+S_1t)^2}\hat{u}_1^s(\boldsymbol{k}, 0) + \hat{u}_3^s(\boldsymbol{k}, 0) \end{bmatrix}, \end{aligned} \tag{A 11}$$

where P and Q are defined by (2.34) and (2.35) respectively.

Appendix B

B.1. *The coefficients in (4.8)*

$$\mathscr{R}_1 = \frac{1}{\pi}\mathrm{Fn}^{-2}(R_u, \beta), \tag{B 1}$$

$$\mathscr{R}_2 = \frac{\beta}{\pi}\mathrm{Fn}^{-2}(R_u, \beta), \tag{B 2}$$

$$\mathscr{B}_1 = \frac{1}{\pi^4}\left(-1 + \frac{2}{R_u}\right)\mathrm{Fn}^{-5}(R_u, \beta), \tag{B 3}$$

$$\mathscr{B}_2 = \frac{2\beta^{5/2}}{\pi^4}\left(1 - \frac{1}{R_u}\right)\mathrm{Fn}^{-5}(R_u, \beta), \tag{B 4}$$

https://doi.org/10.1017/jfm.2016.313 Published online by Cambridge University Press

where the function $\mathrm{Fn}(R_u, \beta)$ is

$$\mathrm{Fn}(R_u, \beta) = \left(-1 + \frac{2}{R_u}\right) + 2\beta^{1/2}\left(1 - \frac{1}{R_u}\right). \tag{B 5}$$

B.2. *The coefficients in (4.11)*

$$\mathscr{R}_1 = \frac{1}{\sqrt{\pi}} \frac{\Gamma\left(\frac{1}{3}\right)}{\Gamma\left(\frac{5}{6}\right)} \mathrm{Fn}^{-1}(R_u, \beta), \tag{B 6}$$

$$\mathscr{R}_2 = \sqrt{\frac{\beta}{\pi}} \frac{\Gamma\left(\frac{1}{3}\right)}{\Gamma\left(\frac{5}{6}\right)} \mathrm{Fn}^{-1}(R_u, \beta), \tag{B 7}$$

$$\mathscr{B}_1 = \frac{55}{36\pi^4} \frac{\Gamma^4\left(\frac{1}{3}\right)}{\Gamma^4\left(\frac{5}{6}\right)} \left(-1 + \frac{2}{R_u}\right) \mathrm{Fn}^{-5}(R_u, \beta), \tag{B 8}$$

$$\mathscr{B}_2 = \frac{55\beta^{5/2}}{18\pi^4} \frac{\Gamma^4\left(\frac{1}{3}\right)}{\Gamma^4\left(\frac{5}{6}\right)} \left(1 - \frac{1}{R_u}\right) \mathrm{Fn}^{-5}(R_u, \beta), \tag{B 9}$$

where $\Gamma(t)$ is the gamma function.

B.3. *The coefficients in (4.15)*

$$\mathscr{L}_0 = \frac{21^2}{\pi} \mathrm{Gn}^{-2}(R_u, \beta), \tag{B 10}$$

$$\mathscr{L}_2 = \frac{21^2\beta}{\pi} \mathrm{Gn}^{-2}(R_u, \beta), \tag{B 11}$$

$$\mathscr{F}_0 = \frac{21^4}{\pi^4} \left(17 + \frac{4}{R_u}\right) \mathrm{Gn}^{-5}(R_u, \beta), \tag{B 12}$$

$$\mathscr{F}_2 = \frac{20 \times 21^4\beta^{5/2}}{\pi^4} \left(\frac{1}{R_u} - 1\right) \mathrm{Gn}^{-5}(R_u, \beta), \tag{B 13}$$

where the function $\mathrm{Gn}(R_u, \beta)$ is

$$\mathrm{Gn}(R_u, \beta) = 4\left(\frac{1}{R_u} + \frac{17}{4}\right) + 10\beta^{1/2}\left(1 - \frac{1}{R_u}\right). \tag{B 14}$$

Unlike Ansatz 1, one must pay attention to the values of β and R_u so as to satisfy the non-negative Hermitian form of $\Phi_{ij}(\boldsymbol{k})$. In this study, we chose $\beta = 1$ for simplicity.

B.4. *The coefficients in (4.16)*

In the von Kármán type, the four coefficients are given by

$$\mathscr{L}_0 = \frac{21}{\sqrt{\pi}} \frac{\Gamma\left(\frac{1}{3}\right)}{\Gamma\left(\frac{5}{6}\right)} \mathrm{Gn}(R_u, \beta)^{-1}, \tag{B 15}$$

$$\mathscr{L}_2 = \frac{21\sqrt{\beta}}{\sqrt{\pi}} \frac{\Gamma\left(\frac{1}{3}\right)}{\Gamma\left(\frac{5}{6}\right)} \mathrm{Gn}(R_u, \beta)^{-1}, \tag{B 16}$$

https://doi.org/10.1017/jfm.2016.313 Published online by Cambridge University Press

$$\mathscr{F}_0 = \frac{1188495}{\pi^4}\frac{\Gamma^4\left(\frac{1}{3}\right)}{\Gamma^4\left(\frac{5}{6}\right)}\left(\frac{1}{R_u}+\frac{17}{4}\right)\mathrm{Gn}^{-5}(R_u,\beta), \tag{B 17}$$

$$\mathscr{F}_2 = \frac{1\,188\,495\beta^{5/2}}{\pi^4}\frac{\Gamma^4\left(\frac{1}{3}\right)}{\Gamma^4\left(\frac{5}{6}\right)}\left(\frac{5}{R_u}-5\right)\mathrm{Gn}^{-5}(R_u,\beta). \tag{B 18}$$

Appendix C

C.1. *Velocity variances*

When the initial velocity fields are in the homogeneous axisymmetric turbulence of Ansatz 1 (model spectrum B), the variances of the perpendicular and parallel components, $\langle u_\parallel^2\rangle$ and $\langle u_\perp^2\rangle$, are given by

$$\langle u_\parallel^2(t)\rangle = \frac{3\pi^{3/2}}{4}\left(\frac{\mathscr{B}_1}{\mathscr{R}_1^{5/2}}+\frac{\mathscr{B}_2}{\mathscr{R}_2^{5/2}}\right)\frac{C^3}{C^2-1}\left[1+(C^2-2)\frac{\tan^{-1}\sqrt{C^2-1}}{\sqrt{C^2-1}}\right], \tag{C 1}$$

$$\begin{aligned}\langle u_\perp^2(t)\rangle \;=\; & \frac{C\pi^{3/2}}{4}\left(\frac{3\mathscr{B}_1}{\mathscr{R}_1^{5/2}}+\frac{\mathscr{B}_2}{\mathscr{R}_2^{5/2}}\right)\\ & +\frac{3\pi^{3/2}}{8}\left(\frac{\mathscr{B}_1}{\mathscr{R}_1^{5/2}}+\frac{\mathscr{B}_2}{\mathscr{R}_2^{5/2}}\right)\frac{C^3}{C^2-1}\left[-1+C^2\frac{\tan^{-1}\sqrt{C^2-1}}{\sqrt{C^2-1}}\right],\end{aligned} \tag{C 2}$$

and the TKE is given by

$$K^s(t) = \frac{C\pi^{3/2}}{4}\left(\frac{3\mathscr{B}_1}{\mathscr{R}_1^{5/2}}+\frac{\mathscr{B}_2}{\mathscr{R}_2^{5/2}}\right)+\frac{3\pi^{3/2}}{4}\left(\frac{\mathscr{B}_1}{\mathscr{R}_1^{5/2}}+\frac{\mathscr{B}_2}{\mathscr{R}_2^{5/2}}\right)C^3\frac{\tan^{-1}\sqrt{C^2-1}}{\sqrt{C^2-1}}. \tag{C 3}$$

When the initial velocity fields are in the homogeneous axisymmetric turbulence of Ansatz 2 (model spectrum C), the variances of the perpendicular and parallel velocity components, $\langle u_\parallel^2\rangle$ and $\langle u_\perp^2\rangle$, are given by

$$\begin{aligned}\langle u_\parallel^2\rangle \;=\; & \frac{3\pi^{3/2}}{4}\frac{\mathscr{F}_0}{\mathscr{L}_0^{5/2}}\left[\frac{C^3}{C^2-1}+C^3\frac{C^2-2}{C^2-1}\frac{\tan^{-1}\sqrt{C^2-1}}{\sqrt{C^2-1}}\right]+\frac{3\pi^{3/2}}{8}\frac{\mathscr{F}_2}{\mathscr{L}_2^{5/2}}\\ & \times\left[-C^3\frac{C^2+8}{(C^2-1)^2}+C^3\frac{5-C^2}{C^2-1}\frac{\tan^{-1}\sqrt{C^2-1}}{\sqrt{C^2-1}}+\frac{9C^3}{(C^2-1)^2}\frac{\tan^{-1}\sqrt{C^2-1}}{\sqrt{C^2-1}}\right],\end{aligned} \tag{C 4}$$

$$\begin{aligned}\langle u_\perp^2\rangle \;=\; & \frac{3\pi^{3/2}}{8}\frac{\mathscr{F}_0}{\mathscr{L}_0^{5/2}}\left[\frac{C^3-2C}{C^2-1}+\frac{C^5}{C^2-1}\frac{\tan^{-1}\sqrt{C^2-1}}{\sqrt{C^2-1}}\right]\\ & +\frac{3\pi^{3/2}}{16}\frac{\mathscr{F}_2}{\mathscr{L}_2^{5/2}}\left[4C+\frac{7C^5+2C^3}{(C^2-1)^2}-\frac{C^5(C^2+8)}{(C^2-1)^2}\frac{\tan^{-1}\sqrt{C^2-1}}{\sqrt{C^2-1}}\right],\end{aligned} \tag{C 5}$$

and the TKE is given by

$$\begin{aligned}K^s(t) \;=\; & \frac{3\pi^{3/2}}{4}\left(\frac{\mathscr{F}_0}{\mathscr{L}_0^5}+\frac{\mathscr{F}_2}{\mathscr{L}_2^5}\right)C+\frac{3\pi^{3/2}}{4}\frac{\mathscr{F}_0}{\mathscr{L}_0^5}C^3\frac{\tan^{-1}\sqrt{C^2-1}}{\sqrt{C^2-1}}\\ & +\frac{3\pi^{3/2}}{16}\frac{\mathscr{F}_2}{\mathscr{L}_2^5}\left(\frac{12C^3}{C^2-1}\frac{\tan^{-1}\sqrt{C^2-1}}{\sqrt{C^2-1}}-\frac{7C^3+5C}{C^2-1}\right).\end{aligned} \tag{C 6}$$

https://doi.org/10.1017/jfm.2016.313 Published online by Cambridge University Press

C.2. *Vorticity variances*

When model spectrum B (the exponential form of Ansatz 1) is used as an initial condition, the variances of perpendicular and parallel vorticity are given by

$$\langle\omega_{\parallel}^2(t)\rangle = \left(\frac{5\pi^{3/2}}{2}\frac{\mathscr{B}_1}{\mathscr{R}_1^{7/2}} + \frac{5\pi^{3/2}}{4}\frac{\mathscr{B}_2}{\mathscr{R}_2^{7/2}}\right)C, \tag{C 7}$$

$$\langle\omega_{\perp}^2(t)\rangle = \frac{\pi^{3/2}C^3}{8}\left(\frac{5\mathscr{B}_1}{\mathscr{R}_1^{7/2}} + \frac{3\mathscr{B}_2}{\mathscr{R}_2^{7/2}}\right) + \frac{15\pi^{3/2}C^3}{8}\left(\frac{\mathscr{B}_1}{\mathscr{R}_1^{7/2}} + \frac{\mathscr{B}_2}{\mathscr{R}_2^{7/2}}\right), \tag{C 8}$$

and the enstrophy is given by

$$\langle\boldsymbol{\omega}^2(t)\rangle = 5\pi^{3/2}\frac{\mathscr{B}_1}{\mathscr{R}_1^{7/2}}\left(C^3 + \frac{C}{2}\right) + \frac{\pi^{3/2}}{2}\frac{\mathscr{B}_2}{\mathscr{R}_2^{7/2}}\left(9C^3 + \frac{5}{2}C\right). \tag{C 9}$$

When model spectrum C (the exponential form of Ansatz 2) is used as an initial condition, the variances of perpendicular and parallel vorticity are given by

$$\langle\omega_{\parallel}^2(t)\rangle = \frac{5\pi^{3/2}C}{2}\left(\frac{\mathscr{F}_0}{\mathscr{L}_0^{7/2}} + \frac{\mathscr{F}_2}{\mathscr{L}_2^{7/2}}\right), \tag{C 10}$$

$$\langle\omega_{\perp}^2(t)\rangle = \frac{5\pi^{3/2}C^3}{2}\frac{\mathscr{F}_0}{\mathscr{L}_0^{7/2}} + \frac{5\pi^{3/2}C^3}{8}\frac{\mathscr{F}_2}{\mathscr{L}_2^{7/2}}, \tag{C 11}$$

and the enstrophy is given by

$$\langle\boldsymbol{\omega}^2(t)\rangle = 5\pi^{3/2}\left(C^3 + \frac{C}{2}\right)\frac{\mathscr{F}_0}{\mathscr{L}_0^{7/2}} + \frac{5\pi^{3/2}}{4}(C^3 + 2C)\frac{\mathscr{F}_2}{\mathscr{L}_2^{7/2}}. \tag{C 12}$$

C.3. *Integral length scales*

When isotropic initial conditions are considered, from (3.6), (3.9) and (5.30), the one-dimensional compressed integral length scales are given by

$$L_{\parallel,\parallel}(t) = L_{11,1}(t) = \frac{4L_f(0)}{3}\frac{C^2-1}{C\left[1 + (C^2-2)\dfrac{\tan^{-1}\sqrt{C^2-1}}{\sqrt{C^2-1}}\right]}, \tag{C 13}$$

$$L_{\parallel,\perp}(t) = L_{11,2}(t) = L_{11,3}(t) = \frac{4L_g(0)}{3}\frac{C^2-1}{C\left[1 + (C^2-2)\dfrac{\tan^{-1}\sqrt{C^2-1}}{\sqrt{C^2-1}}\right]}, \tag{C 14}$$

$$L_{\perp\perp,\perp}(t) = L_{22,2}(t) = L_{33,3}(t) = \frac{4L_f(0)}{3}\frac{1}{\left[1 + \dfrac{C^2}{2(C^2-1)}\left(-1 + C^2\dfrac{\tan^{-1}\sqrt{C^2-1}}{\sqrt{C^2-1}}\right)\right]}, \tag{C 15}$$

$$L_{\perp\perp,\parallel}(t) = L_{22,1}(t) = L_{33,1}(t) = \frac{4L_g(0)}{3}\frac{1}{C\left[1 + \dfrac{C^2}{2(C^2-1)}\dfrac{\tan^{-1}\sqrt{C^2-1}}{\sqrt{C^2-1}}\right]}, \tag{C 16}$$

https://doi.org/10.1017/jfm.2016.313 Published online by Cambridge University Press

$$L_{22,3}(t) = L_{33,2}(t) = \frac{4L_g(0)}{3} \frac{C}{1 + \dfrac{C^2}{2(C^2-1)}(-1+C^2)\dfrac{\tan^{-1}\sqrt{C^2-1}}{\sqrt{C^2-1}}}. \tag{C 17}$$

C.4. *Taylor microscales*

When isotropic initial conditions are considered, the squared Taylor microscales after the compression are given by

$$\lambda^2_{\parallel,\parallel}(t) = \lambda^2_{11,1}(t) = \frac{\lambda_f^2}{5}\frac{C^2-1}{C^2} \frac{1 + (C^2-2)\dfrac{\tan^{-1}\sqrt{C^2-1}}{\sqrt{C^2-1}}}{3\left(-1 + \dfrac{\tan^{-1}\sqrt{C^2-1}}{\sqrt{C^2-1}}\right) + \sqrt{C^2-1}\tan^{-1}\sqrt{C^2-1}}, \tag{C 18}$$

$$\lambda^2_{\parallel,\perp}(t) = \lambda^2_{11,2}(t) = \lambda^2_{11,3}(t) = \frac{4\lambda_g^2}{5}(C^2-1) \frac{1 + (C^2-2)\dfrac{\tan^{-1}\sqrt{C^2-1}}{\sqrt{C^2-1}}}{C^2 + 2 + C^2(C^2-4)\dfrac{\tan^{-1}\sqrt{C^2-1}}{\sqrt{C^2-1}}}, \tag{C 19}$$

$$\begin{aligned} \lambda^2_{\perp\perp,\parallel}(t) &= \lambda^2_{22,1}(t) = \lambda^2_{33,1}(t) \\ &= \frac{4\lambda_g^2}{5} \frac{1 + \dfrac{C^2}{2(C^2-1)}\left(-1 + C^2\dfrac{\tan^{-1}\sqrt{C^2-1}}{\sqrt{C^2-1}}\right)}{C^2\left[\dfrac{2}{3} + \dfrac{C^4}{(C^2-1)^2}\left(2 + \dfrac{1}{C^2} - 3\dfrac{\tan^{-1}\sqrt{C^2-1}}{\sqrt{C^2-1}}\right)\right]}, \end{aligned} \tag{C 20}$$

$$\lambda^2_{\perp\perp,\perp}(t) = \lambda^2_{22,2}(t) = \lambda^2_{33,3}(t) = \frac{\lambda_f^2}{5} \frac{1 + \dfrac{C^2}{2(C^2-1)}\left(-1 + C^2\dfrac{\tan^{-1}\sqrt{C^2-1}}{\sqrt{C^2-1}}\right)}{\dfrac{1}{6} + \dfrac{3}{8}\dfrac{C^4}{(C^2-1)^2}\left[-3 + (C^2+2)\dfrac{\tan^{-1}\sqrt{C^2-1}}{\sqrt{C^2-1}}\right]}, \tag{C 21}$$

$$\lambda^2_{22,3}(t) = \lambda^2_{33,2}(t) = \frac{2\lambda_g^2}{5} \frac{1 + \dfrac{C^2}{2(C^2-1)}\left(-1 + C^2\dfrac{\tan^{-1}\sqrt{C^2-1}}{\sqrt{C^2-1}}\right)}{\dfrac{1}{2} + \dfrac{1}{8}\dfrac{C^4}{(C^2-1)^2}\left[-3 + (C^2+2)\dfrac{\tan^{-1}\sqrt{C^2-1}}{\sqrt{C^2-1}}\right]}. \tag{C 22}$$

REFERENCES

AGUI, J. H., BRIASSULIS, G. & ANDREOPOULOS, J. 2005 Studies of interactions of a propagating shock wave with decaying grid turbulence: velocity and vorticity fields. *J. Fluid Mech.* **524**, 143–195.

ANDREOPOULOS, J., AGUI, J. H. & BRIASSULIS, G. 2000 Shock wave–turbulence interaction. *Annu. Rev. Fluid Mech.* **524**, 309–345.

https://doi.org/10.1017/jfm.2016.313 Published online by Cambridge University Press

ARMSTRONG, J. W., RICKETT, B. J. & SPRANGER, S. R. 1995 Electro density power spectrum in the local interstellar medium. *Astrophys. J.* **443**, 209–221.

BARRE, S., ALEM, D. & BONNET, J. P. 1996 Experimental study of a normal shock/homogeneous turbulence interaction. *AIAA J.* **34**, 968–974.

BATCHELOR, G. K. 1946 The theory of axisymmetric turbulence. *Proc. R. Soc. Lond.* A **186**, 480–502.

BATCHELOR, G. K. 1953 *The Theory of Homogeneous Turbulence*. Cambridge University Press.

BERTOGLIO, J. P., BATAILLE, F. & MARION, J. D. 2001 Two–point closures for weakly compressible turbulence. *Phys. Fluids* **13**, 290–310.

BRIASSULIS, G., AGUI, J. H., ANDREOPOULOS, J. & WATKINS, C. B. 1996 A shock tube research facility for high-resolution measurements of compressible turbulence. *Exp. Therm. Fluid Sci.* **13**, 430–446.

CAMBON, C., MANSOUR, N. N. & GODEFEFERD, F. S. 1997 Energy transfer in rotating turbulence. *J. Fluid Mech.* **337**, 303–332.

CAMBON, C. & TEISSÈDRE, C. 1985 Application des harmoniques sphériques à la représentation et au calcul des grandeurs cinématiques en turbulence homogène anisotrope. *C. R. Acad. Sci. Paris* II **301**, 65–68.

CHANDRASEKHAR, S. 1950 The theory of axisymetric turbulence. *Phil. Trans. R. Soc. Lond.* A **242**, 557–577.

CRAIK, A. D. D. & CRIMINALE, W. O. 1986 Evolution of wavelike disturbances in shear flows: a class of exact solutions of Navier–Stokes equations. *Proc. R. Soc. Lond.* A **406**, 13–26.

DAVIDSON, P. A. 2004 *Turbulence: An Introduction for Scientists and Engineers*. Oxford University Press.

DURBIN, P. A. & ZEMAN, O. 1992 Rapid distortion theory for homogeneous compressed turbulence with application to modelling. *J. Fluid Mech.* **242**, 349–370.

GRUBE, N. E., TAYLOR, E. M. & MARTIN, M. P. 2011 Numerical investigation of shock wave/isotropic turbulence interaction. In *49th AIAA Aerospace Sciences Meeting*.

HANAZAKI, H. & HUNT, J. C. R. 1996 Linear processes in unsteady stably stratified turbulence. *J. Fluid. Mech.* **318**, 303–337.

HANAZAKI, H. & HUNT, J. C. R. 2004 Structure of unsteady stably stratified turbulence with mean shear. *J. Fluid. Mech.* **507**, 1–42.

HANNAPPEL, R. & FRIEDRICH, R. 1995 Direct numerical simulation of a Mach 2 shock interacting with isotropic turbulence. *Appl. Sci. Res.* **54**, 205–221.

HONKAN, A. & ANDREOPOULOS, J. 1992 Rapid compression of grid-generated turbulence by a moving shock wave. *Phys. Fluids* **4**, 2562–2572.

HUNT, J. C. R. & CARRUTHERS, D. J. 1990 Rapid distortion theory and the 'problems' of turbulence. *J. Fluid Mech* **212**, 497–532.

HUNT, J. C. R. & KEVLAHAN, N. 1993 Rapid distortion theory and the structure of turbulence. In *New Approaches and Concepts in Turbulence*, pp. 285–316.

JACQUIN, L., CAMBON, C. & BLIN, E. 1993 Turbulence amplification by a shock wave and rapid distortion theory. *Phys. Fluids* **5**, 2539–2550.

KELLER, J. & MERZKIRCH, W. 1990 Interaction of a normal shock wave with a compressible turbulent flow. *Exp. Fluids* **8**, 241–248.

KEVLAHAN, N. K. R. 1997 The vorticity jump across a shock in a non-uniform flow. *J. Fluid Mech.* **341**, 371–384.

KEVLAHAN, N. K. R. & HUNT, J. C. R. 1997 Nonlinear interactions in turbulence with strong irrotational straining. *J. Fluid Mech.* **337**, 333–364.

KITAMURA, T., NAGATA, K., SAKAI, Y., SASOH, A., TERASHIMA, O., SAITO, H. & HARASAKI, T. 2014 On invariants in grid turbulence at moderate Reynolds numbers. *J. Fluid Mech.* **738**, 378–406.

KROGSTAD, P. Å. & DAVIDSON, P. A. 2010 Is grid turbulence Saffman turbulence? *J. Fluid Mech.* **642**, 373–394.

LARSSON, J., BERMEJO-MORENO, I. & LELE, S. K. 2013 Reynolds- and Mach-number effects in canonical shock–turbulence interaction. *J. Fluid Mech.* **717**, 293–321.

https://doi.org/10.1017/jfm.2016.313 Published online by Cambridge University Press

LARSSON, J. & LELE, S. K. 2009 Direct numerical simulation of canonical shock/turbulence interaction. *Phys. Fluids* **21**, 126101.

LEE, L., LELE, S. K. & MOIN, P. 1993 Direct numerical simulation of isotropic turbulence interacting with a weak shock wave. *J. Fluid Mech.* **251**, 533–562.

LEE, L., LELE, S. K. & MOIN, P. 1997 Interaction of isotropic turbulence with shock wave: effect of shock strength. *J. Fluid Mech.* **340**, 225–247.

MAHESH, K., LELE, S. K. & MOIN, P. 1994 The response of anisotropic turbulence to rapid homogeneous one-dimensional compression. *Phys. Fluids* **6**, 1052–1062.

MAHESH, K., LELE, S. K. & MOIN, P. 1997 The influence of entropy fluctuations on the interaction of turbulence with a shock wave. *J. Fluid Mech.* **84**, 497–516.

MARION, J. D., BERTOGLIO, J. P. & MATHIEU, J. 1988 Spectral study of weakly compressible isotropic turbulence: Part I: direct interaction approximation. *C. R. Acad. Sci. Paris* II **307**, 1487–1492.

MIVILLE-DESCHENES, M. A., JONCAS, G., FALGARONE, E. & BOULANGER, F. 2003 High resolution 21 cm mapping of the Ursa Major Galatic cirrus: power spectra of the high-latitude H I gas. *Astron. Astrophys.* **411**, 109–121.

NAGATA, K., WONG, H., HUNT, J. C. R., SAJJADI, S. G. & DAVIDSON, P. A. 2006 Weak mean flows induced by anisotropic turbulence impinging onto planar and undulating surfaces. *J. Fluid Mech.* **556**, 329–360.

RIBNER, H. S. & TUCKER, M. 1953 Spectrum of turbulence in a contracting stream. *NACA Rep.* 1113.

SAGAUT, P. & CAMBON, C. 2008 *Homogeneous Turbulence Dynamics*. Cambridge University Press.

SREENIVASAN, K. R. & NARASIMHA, R. 1978 Rapid distortion of axisymmetric turbulence. *J. Fluid Mech.* **84**, 497–516.

https://doi.org/10.1017/jfm.2016.313 Published online by Cambridge University Press